DIGITAL AUTOLAND SYSTEM FOR UNMANNED AERIAL VEHICLES

A Thesis

by

THOMAS WILLIAM WAGNER, JR.

Submitted to the Office of Graduate Studies of
Texas A&M University
in partial fulfillment of the requirements for the degree of

MASTER OF SCIENCE

May 2007

Major Subject: Aerospace Engineering

DIGITAL AUTOLAND SYSTEM FOR UNMANNED AERIAL VEHICLES

A Thesis

by

THOMAS WILLIAM WAGNER, JR.

Submitted to the Office of Graduate Studies of
Texas A&M University
in partial fulfillment of the requirements for the degree of

MASTER OF SCIENCE

Approved by:

Chair of Committee,	John Valasek
Committee Members,	Thomas Strganac
	Reza Langari
Head of Department,	Helen L. Reed

May 2007

Major Subject: Aerospace Engineering

ABSTRACT

Digital Autoland System for Unmanned Aerial Vehicles. (May 2007)
Thomas William Wagner, Jr., B.S., Texas A&M University
Chair of Advisory Committee: Dr. John Valasek

Autoland controllers are prevalent for both large and small/micro unmanned aerial vehicles, but very few are available for medium sized unmanned aerial vehicles. These vehicles tend to have limited sensors and instrumentation, yet must possess good performance in the presence of modeling uncertainties, and exogenous inputs such as turbulence. Quantitative Feedback Theory is an attractive control methodology for this application, since it provides good performance and robustness for systems with structured model uncertainties. It has been successfully applied to many aircraft problems, but not to automatic landing, and only inner-loop synthesis has been presented in the literature. This paper describes the synthesis and development of an automatic landing controller for medium size unmanned aerial vehicles, using discrete Quantitative Feedback Theory. Controllers for the localizer, glideslope tracker, and automatic flare are developed, with a focus on the outer-loops synthesis. Linear, non real-time six degree-of-freedom Monte Carlo simulation is used to compare the Quantitative Feedback Theory controller to a baseline Proportional-Integral controller in several still air and turbulent landing scenarios. The Quantitative Feedback Theory controller provides performance similar to the Proportional-Integral controller in still and in turbulent air. Both controllers show similar robustness to turbulence, but the Quantitative Feedback Theory controller provides significantly better robustness to model uncertainties in turbulent air as well as to sensor characteristics in turbulence. Based on the results of the paper, the QFT controller is a promising candidate for an

autoland controller.

To my parents, for always believing in me and letting me chase my dreams

ACKNOWLEDGMENTS

I would like to acknowledge and thank the many people who have helped in the successful completion of this thesis, most notably Dr. John Valasek, who has been a great professor, advisor, and mentor throughout my graduate career. Without his patience and dedication this work would not have been possible. The assistance of my thesis committee in taking the time to review the technical aspects of this research is acknowledged and greatly appreciated. Thanks to all of my professors from which I have learned so much more than I thought possible. I am also very grateful to all of my wonderful friends who have made graduate school so memorable and rewarding. Because of them, I have managed to keep my sanity while pursuing this degree. Finally, I would like to thank my parents and family who have always supported me no matter what I've wanted to do. Without their love and support, none of this would be possible. Thanks and Gig 'Em.

TABLE OF CONTENTS

CHAPTER Page

LIST OF TABLES

LIST OF FIGURES

FIGURE Page

FIGURE Page

CHAPTER I

INTRODUCTION

The landing phase of a flight presents unique challenges to designing a flight control system for the approach and touchdown of an aircraft. Atmospheric disturbances such as wind and turbulence and sensor noise from various approach types require a controller to reject external disturbances introduced to the system. Due to preliminary modeling limitations, parameter uncertainties are present in a system, and the controller must be insensitive to these uncertainties. In addition to parameter insensitivity and disturbance rejection, an autoland controller must provide good performance to provide an accurate approach and smooth touchdown in order to prevent damage to the aircraft. Although this research is for unmanned aerial vehicles, the work and results found from this paper apply for piloted aircraft as well. The techniques developed in this paper can easily be extended to general aviation aircraft, military aircraft, or commercial aircraft.

For any automatic landing system, regardless of the control methodology used, the following requirements must be met:

- Provide good performance during approach and landing such that aircraft safely touches down without damage to the aircraft
- Offer robustness to model uncertainties, external disturbances such as wind and turbulence, and sensor characteristics
- Give repeatable results for a variety of possible aircraft configurations and environmental conditions

---

The journal model is *IEEE Transactions on Intelligent Transportation Systems.*

The autoland problem has been successfully approached by a variety of methods. References [1] and [2] used Proportional-Integral (PI) controllers for the automatic landing of large transport aircraft. Fuzzy logic has been used to solve the autoland problem for a medium sized transport aircraft in Reference [3], and neural networks have been used for a large transport aircraft in Reference [4]. Mixed H_2/H_∞ control was applied to the automatic landing of an F-14 aircraft in Reference [5]. All of the aforementioned techniques were applied to larger, manned vehicles. Reference [6] applies the linear-quadratic technique to the automatic landing of a small Unmanned Aerial Vehicle (UAV), and Reference [7] develops a fault tolerant automatic landing controller for the Heron UAV, which is a medium size UAV. Several autoland systems exist for small or micro UAVs [8] [9], and vehicle specific controllers exist for the automatic landing of large UAVs [10] [11] [12] . Very few systems are available for medium size UAVs. Sierra Nevada Corporation offers an automatic landing system for medium size UAVs, but this system is expensive and requires additional ground equipment [13].

Quantitative Feedback Theory (QFT) is a design technique which offers robust performance amidst structured model uncertainties. This technique can be applied to Multiple Input Single Output (MISO) systems and Multiple Input Multiple Output (MIMO) systems in both the time and frequency domains [14] [15]. QFT has been successfully applied to a number of vehicles, both manned and unmanned. QFT was utilized for inner-loop stability control of various aircraft such as the F-15, F-16, and X-29 [16]. A pitch attitude hold controller was developed for both a fighter jet and a business jet in Reference [17], and a lateral/directional flight control system was designed in Reference [18] for a large transport aircraft. Reference [19] documents the first flight test of a QFT longitudinal controller on a small UAV, and Reference [20] documents the design and flight test of a QFT pitch rate stability augmentation

system for a small UAV.

Most research to date in QFT has focused on inner-loop flight control, with little or no work on synthesis of the outer-loops. The unique specific contributions of this paper are the development of a QFT controller using direct digital design for the approach and automatic landing of a medium size UAV, and detailing of the synthesis and interactions of the outer-loops. Performance of the digital QFT controller is quantified by Monte Carlo simulation comparison with a baseline Proportional-Integral (PI) approach and automatic landing controller. A detailed parametric study on the effect of model uncertainties, turbulence, and winds is also presented.

The paper is organized as follows. Chapter II introduces and details the specifics of the approach and landing problem. Chapter III describes the development of a non-parametric aircraft model using system identification, and verifies the identified model. Chapter IV presents the digital controller synthesis, describing the development of the QFT and PI controllers. Non-real time simulation results are reported in Chapter VI. Finally, conclusions are presented in Chapter VII and recommendations are presented in Chapter VIII.

CHAPTER II

PROBLEM STATEMENT AND DEFINITION

The purpose of this chapter is to describe the approach and landing problem posed for this research. As noted in Chapter I, the automatic landing consists of intercepting a lateral and vertical beam and tracking the guidance provided to a specified height above the runway, where a flare maneuver is performed. It is assumed that a guidance system is available to provide lateral and vertical guidance to the start of the flare. Fig. 1 from Reference [21] details the geometry used to determine deviations from the lateral and vertical beam, and Fig. 2 illustrates the geometry of the flare maneuver. The control laws were developed for a Category (CAT) IIIc (no requirements on cloud ceiling or visibility) Instrument Landing System (ILS), although the techniques can easily be extended to any guidance system, as will be shown in Chapter VI. Since ILS was initially assumed for control law design, the lateral beam will be referred to as the localizer, and the vertical beam will be referred to as the glideslope.

The localizer consists of a transmitter stationed at the far end of the runway which sends out a signal that is approximately 5 deg wide (beamwidth) and is centered on the runway centerline. Typical interception occurs when the aircraft flies at a heading to intercept the localizer at a range of 6-10 nm from the runway threshold. The glideslope consists of a transmitter stationed approximately 1,000 ft from the approach end of the runway, which sends a beam that is elevated approximately 3 deg above the horizon and approximately 1.4 deg wide. The glideslope is intercepted by flying straight and level at a specified altitude until flying through the beam at a range of 4-5 nm from the runway threshold, at which time the beam is tracked down to the flare height [22].

Another component in the automatic flare system is the airspeed command and

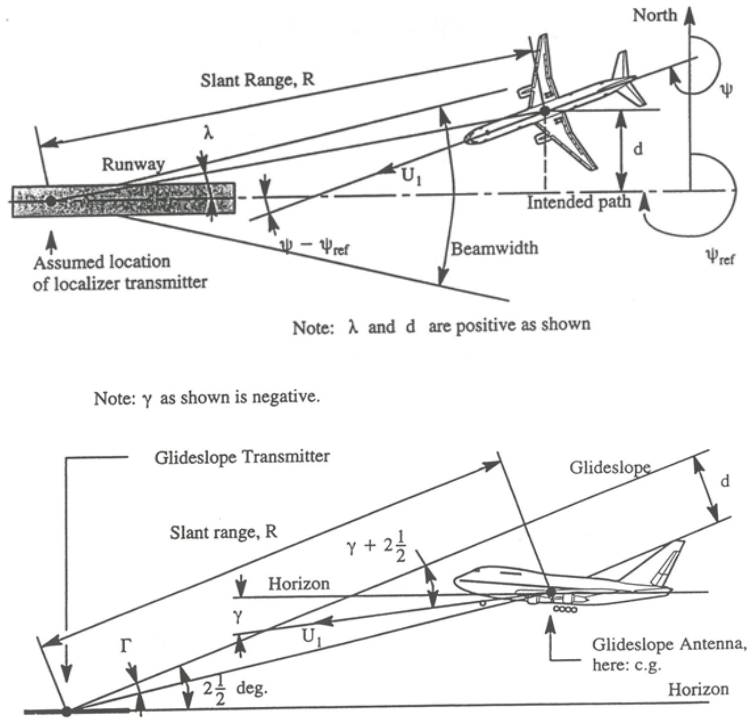

Fig. 1. Localizer and Glideslope Tracking Geometry

hold, which controls the airspeed of the aircraft using the throttle. During the approach, the airspeed is maintained at the specified approach speed, and after passing through the flare height, the airspeed is reduced to just above the stall speed before touchdown. If airspeed is not properly maintained, the aircraft will have difficulty tracking the glideslope, and during the flare, the aircraft will either float down the runway or touch down with a higher velocity than normal, which could damage the aircraft.

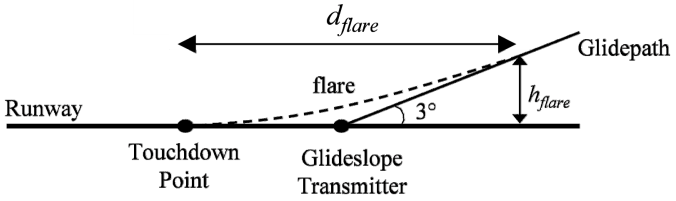

Fig. 2. Autoflare Geometry

To provide a smooth transition from the flare height to the runway, an exponential function is given as a reference trajectory, which has the form shown in the following equation.

$$\dot{h} = h_{flare} e^{-\frac{1}{\tau}} \tag{2.1}$$

In the above equation, h_{flare} is the height at which the flare maneuver is started, and τ is a time constant used to shape the trajectory. Following the method of Reference [2], the trajectory was shaped for a touchdown point 1,000 ft beyond the start of the flare, which leads to a $\tau = 1.99$ sec, and $h_{flare} = 17.47$ ft. This is reasonable for an aircraft of this size because most general aviation aircraft start to flare between 10 ft and 30 ft above the ground.

It is desired for the aircraft to intercept the localizer and glideslope and track these beams to the runway centerline and to the flare height. After reaching the flare height, the vehicle should touch down with a small vertical velocity to prevent damage to the aircraft, and it is also desired to minimize the distance traveled down the runway to prevent running off the runway. Reference [21] states that damage occurs at a touchdown velocity of greater than 10 ft/sec and "hard" landings occur at a touchdown velocity of greater than 6 ft/sec. Additional considerations should be made to ensure that the pitch attitude angle is greater than the nominal pitch attitude angle when the aircraft is resting on the ground to prevent "wheel-barrowing"

or landing on the nose gear first.

CHAPTER III

AIRCRAFT MODEL

The non-parametric aircraft model used for synthesis and simulation of the approach and flare control laws was derived using system identification of a real-time, high fidelity nonlinear six degree-of-freedom flight simulator. The simulation model is a Rockwell Commander 700, a light twin-engine general aviation aircraft shown in Fig. 3. This aircraft model is implemented in the Engineering Flight Simulator of Texas A&M's Flight Simulation Laboratory.

Fig. 3. Rockwell Commander 700

This vehicle is used because it is desired to implement and test the control laws in the simulator. Although this vehicle is much larger than a medium size UAV, it is assumed here that the dynamics of this vehicle are generally representative to those of a medium size UAV. Since a high fidelity nonlinear model exists, Observer/Kalman filter Identification (OKID) [23] is used to determine a linear time-invariant (LTI) state-space representation of the C700. The linear state-space model is in the form

$$\begin{aligned} \dot{\boldsymbol{x}} &= A\boldsymbol{x} + B\boldsymbol{u} \quad \text{state equation} \\ \boldsymbol{y} &= C\boldsymbol{x} + D\boldsymbol{u} \quad \text{output equation} \end{aligned} \tag{3.1}$$

where $\boldsymbol{x} \in \mathbb{R}^{n\times 1}$ is a state vector with n states, $\boldsymbol{u} \in \mathbb{R}^{m\times 1}$ is an input vector with m inputs, $\boldsymbol{y} \in \mathbb{R}^{p\times 1}$ is an output vector with p outputs, $A \in \mathbb{R}^{n\times n}$ is a plant matrix, $B \in \mathbb{R}^{n\times m}$ is a control distribution matrix, and $C \in \mathbb{R}^{p\times n}$ and $D \in \mathbb{R}^{p\times m}$ are matrices that determine the elements of the output vector. The dynamic models are expressed in the stability axis system, which is depicted in Fig. 4.

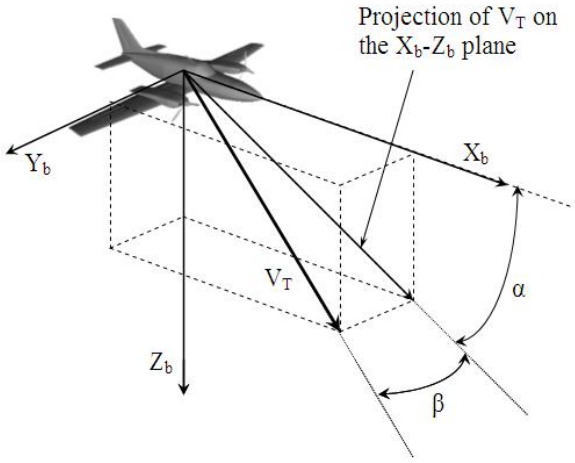

Fig. 4. Definition of Body Axis System and Aerodynamic Angles

For the identification effort, the aircraft was in the power approach configuration (gear down, flaps down) at the flight condition listed in Table I [24].

Table I. C700 Power Approach Flight Condition

Parameter	Value	Units
Altitude, h_1	1,000	ft
Airspeed, U_1	151.9	ft/sec
Pitch Attitude, θ_1	0.66	deg
Angle-of-Attack, α_1	0.65	deg
Elevator Deflection, δ_{e_1}	1.996	deg
Throttle Setting, δ_{T_1}	75.26	%

A. Lateral/Directional Model

The states of the lateral/directional model are sideslip angle (β), body axis roll rate (p), body axis yaw rate (r), and body axis roll attitude angle (ϕ). Aileron deflection (δ_a) and rudder deflection (δ_r) are the lateral/directional controls. A 3-2-1-1 aileron maneuver followed immediately by a 3-2-1-1 rudder maneuver was used to perturb the lateral/directional model. The 3-2-1-1 maneuver involves a series of control inputs where the control is commanded to one side for three seconds, the opposite side for two seconds, and finally, a one second control input in each direction. The identified lateral/directional model is shown in (3.2).

$$\begin{bmatrix} \dot{\beta} \\ \dot{p} \\ \dot{r} \\ \dot{\phi} \end{bmatrix} = \begin{bmatrix} -0.2187 & 0.0319 & -1.0175 & 0.1754 \\ 1.1195 & -2.1647 & 0.1438 & -0.0031 \\ 3.8280 & -0.6813 & -0.2509 & 0.0031 \\ 0.0294 & 0.9225 & -0.0449 & -0.0016 \end{bmatrix} \begin{bmatrix} \beta \\ p \\ r \\ \phi \end{bmatrix} + \begin{bmatrix} 0.0192 & 0.0165 \\ -2.0338 & 0.2634 \\ -0.0209 & -0.7004 \\ -0.1513 & 0.0034 \end{bmatrix} \begin{bmatrix} \delta_a \\ \delta_r \end{bmatrix} \tag{3.2}$$

The eigenvalues and modes of this system are

$$\begin{array}{lllllllll} \lambda_{dr} & = & -0.312 \pm 1.92i & \lambda_{roll} & = & -2.02 & \lambda_{sprl} & = & 0.0067 \\ \zeta_{dr} & = & 0.160 & T_{roll} & = & 0.50 \text{ sec} & T_{sprl} & = & -149.25 \text{ sec} \\ \omega_{n_{dr}} & = & 1.95 \text{ rad/sec} & & & & & & \end{array} \tag{3.3}$$

The model exhibits standard modes, with an unstable spiral mode. This is not a great concern since many aircraft have an unstable spiral mode, and this instability is often stabilized using feedback.

To verify the identified model, identical control inputs were given to both the nonlinear simulator model and the identified model. To properly verify the model found from OKID, a different input should be used. Since a 3-2-1-1 input was given for identification doublets were used for verification. First an aileron doublet was given, followed by a rudder doublet. Model verification plots are displayed in Fig. 5 for the lateral/directional identified model and shows that the identified model compares well with the simulator for all states. It is concluded that the identified model is representative of the actual dynamics of the simulator.

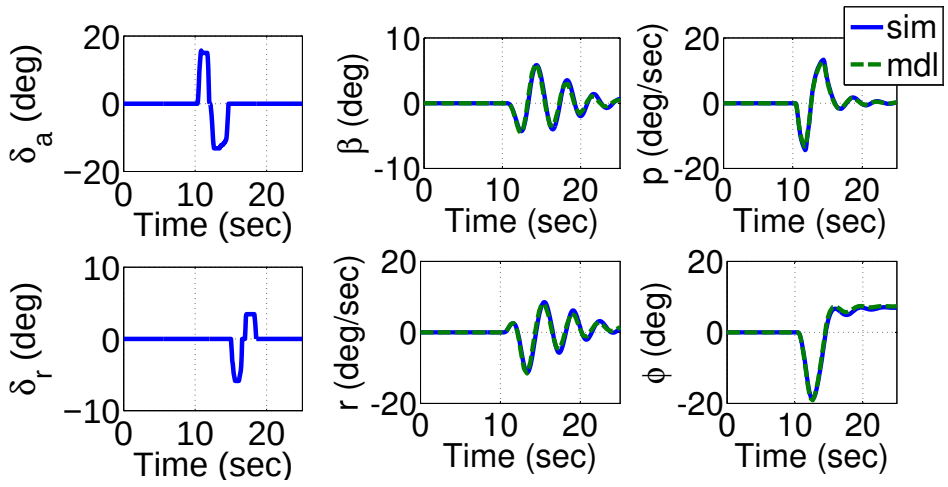

Fig. 5. Lateral/Directional Model Verification

A first-order actuator model with a time constant of $\tau = 0.1$ sec is assumed for the aileron and rudder. Here δ is the control surface position, δ_c is the commanded control surface position, and s is the Laplace variable.

$$\frac{\delta}{\delta_c} = \frac{1/\tau}{s + 1/\tau} \tag{3.4}$$

B. Longitudinal Model

The longitudinal model was identified in the same manner as the lateral/directional model described above. The perturbed states of the longitudinal state-space model are aircraft total velocity (u), angle-of-attack (α), body axis pitch rate (q), and pitch attitude angle (θ). A throttle doublet followed by an elevator doublet was used to identify the longitudinal model. The identified model found from OKID is

$$\begin{bmatrix} \dot{u} \\ \dot{\alpha} \\ \dot{q} \\ \dot{\theta} \end{bmatrix} = \begin{bmatrix} -0.2371 & -0.3715 & -0.0518 & -0.6304 \\ -0.1394 & -1.0602 & 0.9127 & -0.0230 \\ 0.0918 & 0.2402 & -2.0719 & -0.1316 \\ 0.0129 & 0.0450 & 0.8722 & -0.0080 \end{bmatrix} \begin{bmatrix} u \\ \alpha \\ q \\ \theta \end{bmatrix} + \begin{bmatrix} -0.4012 & 0.1241 \\ -0.6219 & 0.0000 \\ -7.1121 & -0.0036 \\ -0.6369 & 0.0003 \end{bmatrix} \begin{bmatrix} \delta_e \\ \delta_T \end{bmatrix} \tag{3.5}$$

with dynamic modes and eigenvalues

$$\begin{array}{lllllllll} \lambda_{3rd} & = & -0.138 \pm 0.136i & \lambda_3 & = & -0.861 & \lambda_4 & = & -2.24 \\ \zeta_{3rd} & = & 0.712 & T_3 & = & 1.16 \text{ sec} & T_4 & = & 0.45 \text{ sec} \\ \omega_{n_{3rd}} & = & 0.194 \text{ rad/sec} & & & & & & \end{array} \tag{3.6}$$

The dynamic modes show that this system has a third oscillatory mode and two first-order stable modes. Although not standard for aircraft, the third oscillatory mode usually does not present a problem for control law design. To verify the identified model, the same method was used as for the lateral/directional case. Since doublets were used to identify the model, 3-2-1-1 inputs were used for verification. A throttle 3-2-1-1 maneuver was given to the system followed by an elevator 3-2-1-1 maneuver. Fig. 6 displays the verification of the identified longitudinal model and shows that the longitudinal model agrees well with the simulator model. There is a discrepancy in airspeed between 10 sec and 20 sec. The frequency content matches well, but the amplitude does not. This difference is not of great concern because the airspeed will be controlled by the throttle, and during the time period in which throttle is input

to the system, the airspeed matches well for both frequency and amplitude.

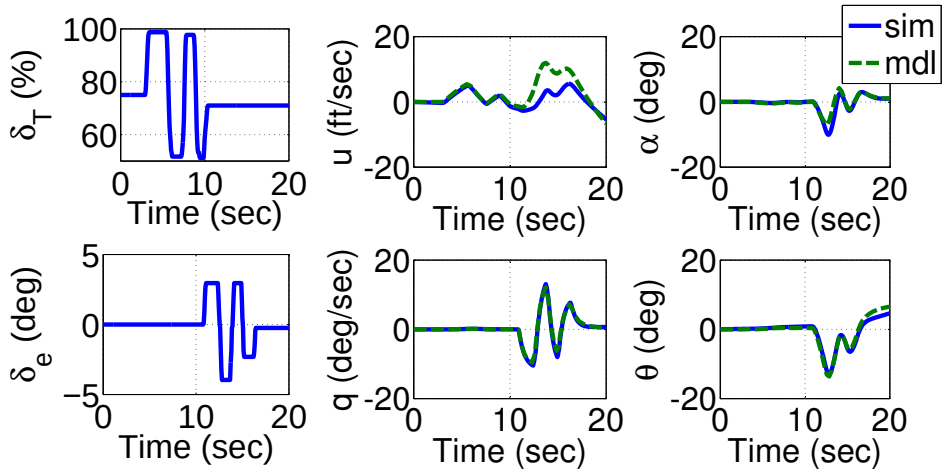

Fig. 6. Longitudinal Model Verification

A first-order actuator model is assumed for the elevator and throttle dynamics. The elevator was assumed to have a 0.1 sec time constant, and the throttle was assumed to have a 0.33 sec time constant. An engine lag of 1 sec was also added to the system to increase the realism of the aircraft model.

C. Ground Effect Modeling

As the aircraft descends toward the ground, the trailing edge vortex development is disrupted by the ground, which tends to increase the upwash on the wing surface such that the lift coefficient, C_L, is increased and the induced drag coefficient, C_{D_i}, is decreased. It is assumed that the decrease in drag is small, and thus the focus of the ground effect modeling will be centered on the increase in lift. This increase in lift can be viewed as an increase in the aircraft lift curve slope, C_{L_α}, and a decrease in the zero-lift angle-of-attack, α_0. From Reference [25], the change in α_0 can be approximated by (3.7).

$$\Delta\alpha_0 = \frac{t}{c}\left[-0.1177\frac{1}{(h/c)^2} + 3.5655\frac{1}{(h/c)}\right] \tag{3.7}$$

In (3.7), $\frac{t}{c}$ is the thickness ratio of the aircraft, and $\frac{h}{c}$ is the aircraft height above the ground normalized by the mean aerodynamic chord. The increase in C_{L_α} can be expressed as in (3.8).

$$C_{L_{\alpha_{IGE}}} = \frac{2\pi AR_{eff}}{2 + \sqrt{AR_{eff}^2\left(1 + tan^2\Lambda_{c/2}\right) + 4}} \tag{3.8}$$

In (3.8), $\Lambda_{c/2}$ is the mid-chord sweep angle and AR_{eff} is the effective aspect ratio, which can be approximated from Fig. 7.

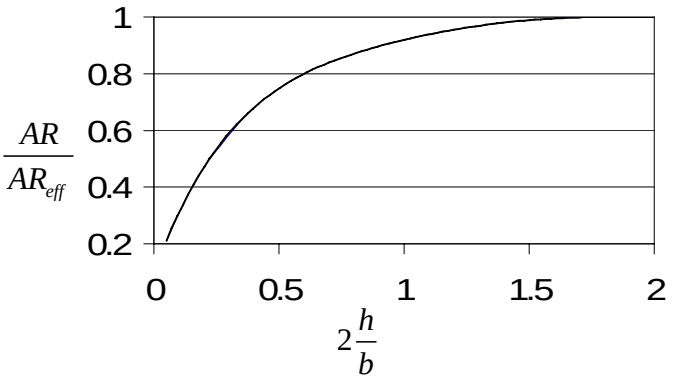

Fig. 7. Determination of Effective Aspect Ratio

From Fig. 7, the horizontal axis is the aircraft height above the ground normalized by the wingspan of the aircraft, and the vertical axis is the ratio between the aircraft aspect ratio and the effective aspect ratio of the aircraft when it is in ground effect. The curve in the figure can be approximated by (3.9).

$$\begin{aligned}\frac{AR}{AR_{eff}} &= -0.0235\left(2\frac{h}{b}\right)^6 + 0.2803\left(2\frac{h}{b}\right)^5 - 1.2428\left(2\frac{h}{b}\right)^4 + 2.7442\left(2\frac{h}{b}\right)^3 \\ &\quad -3.3818\left(2\frac{h}{b}\right)^2 + 2.447\left(2\frac{h}{b}\right) + 0.096 \end{aligned} \tag{3.9}$$

D. Turbulence Modeling

One focus of this paper is to analyze the robustness of the control laws to turbulence. Turbulence is added to the system using the Dryden Wind Turbulence block of the MATLAB Aerospace blockset [26]. This model uses the Dryden spectral representation to add turbulence to the model by passing band-limited white noise through forming filters as defined in MIL-STD-1797A [27], which are shown in (3.10) and (3.11).

$$H_u(s) = \sigma_u\sqrt{\frac{2L_u}{\pi V}}\frac{1}{1+\frac{L_u}{V}s} \tag{3.10a}$$

$$H_v(s) = \sigma_v\sqrt{\frac{2L_v}{\pi V}}\frac{1+\frac{2\sqrt{3}L_v}{V}s}{(1+\frac{2L_v}{V}s)^2} \tag{3.10b}$$

$$H_w(s) = \sigma_w\sqrt{\frac{2L_w}{\pi V}}\frac{1+\frac{2\sqrt{3}L_w}{V}s}{(1+\frac{2L_w}{V}s)^2} \tag{3.10c}$$

$$H_p(s) = \sigma_w\sqrt{\frac{0.8}{V}}\frac{(\frac{\pi}{4b})^{1/6}}{(2L_w)^{1/3}(1+(\frac{4b}{\pi V})s)} \tag{3.11a}$$

$$H_q(s) = \frac{\frac{s}{V}}{1+(\frac{4b}{\pi V})s}H_w(s) \tag{3.11b}$$

$$H_r(s) = \frac{\frac{s}{V}}{1+(\frac{3b}{\pi V})s}H_v(s) \tag{3.11c}$$

In the turbulence transfer functions, V is the airspeed of the aircraft, b is the aircraft

wingspan, s is the Laplace variable, L is the turbulence scale length, and σ is the turbulence intensity. The turbulence scale length is based on altitude above the ground, h, as shown in (3.12).

$$L_u(s) = \frac{h}{(0.177 + 0.000823h)^{1.2}} \tag{3.12a}$$

$$L_v(s) = \frac{h}{2(0.177 + 0.000823h)^{1.2}} \tag{3.12b}$$

$$L_w(s) = \frac{h}{2} \tag{3.12c}$$

The turbulence intensity is based on altitude above the ground, h, and the wind speed at 20 feet, W_{20}, as displayed in (3.13)

$$\sigma_u(s) = \frac{0.1W_{20}}{(0.177 + 0.000823h)^{0.1}} \tag{3.13a}$$

$$\sigma_v(s) = \frac{0.1W_{20}}{(0.177 + 0.000823h)^{0.4}} \tag{3.13b}$$

$$\sigma_w(s) = 0.1W_{20} \tag{3.13c}$$

For light turbulence, $W_{20} = 15$ kts, for moderate turbulence, $W_{20} = 30$ kts, and for severe turbulence, $W_{20} = 45$ kts. After passing white noise through the forming filters, the turbulence is added as an exogenous input to the aircraft.

E. Model Uncertainties

High fidelity, nonlinear, six degree-of-freedom models are not available for all vehicles, so typically parametric models are used to create a LTI state-space model. Stability and control derivatives are used to construct the state-space model according to the linearized equations of motion, using Taylor series expansions. Assuming that the

longitudinal and lateral/directional dynamics are decoupled, which is the case for $\phi = 0$, the linearized equations of motion for lateral/directional axis takes the form shown in (3.14).

$$\begin{bmatrix} 1 & 0 & 0 & 0 \\ 0 & 1 & -\frac{I_{xz}}{I_{xx}} & 0 \\ 0 & -\frac{I_{xz}}{I_{zz}} & 1 & 0 \\ 0 & 0 & 0 & 1 \end{bmatrix} \begin{bmatrix} \dot{\beta} \\ \dot{p} \\ \dot{r} \\ \dot{\phi} \end{bmatrix} = \begin{bmatrix} \frac{Y_\beta}{U_1} & \frac{Y_p}{U_1} & \frac{Y_r}{U_1} + 1 & \frac{gcos(\theta_1)}{U_1} \\ L_\beta & L_p & L_r & 0 \\ N_\beta + N_{T_\beta} & N_p & N_r & 0 \\ 0 & 1 & tan(\theta_1) & 0 \end{bmatrix} \begin{bmatrix} \beta \\ p \\ r \\ \phi \end{bmatrix} + \begin{bmatrix} \frac{Y_{\delta_a}}{U_1} & \frac{Y_{\delta_r}}{U_1} \\ L_{\delta_a} & L_{\delta_r} \\ N_{\delta_a} & N_{\delta_r} \\ 0 & 0 \end{bmatrix} \begin{bmatrix} \delta_a \\ \delta_r \end{bmatrix} \tag{3.14}$$

The parameters in (3.14) result from dimensionalizing the stability derivatives. Each of these terms is associated with a stability derivative; for example, N_β is a function of C_{n_β}, and Y_{δ_r} is a function of $C_{y_{\delta_r}}$. Because of limitations on preliminary modeling of aircraft, uncertainties exist for all of the stability and control derivatives. Table II from Reference [28] outlines the relative importance of each stability derivative, with 10 as the most important and 1 as the least important, and the accuracy to which it can be predicted by preliminary modeling techniques [29].

From Table II, it can be seen that control power derivatives are not included because data is not readily available for the uncertainty of these derivatives. Since the lateral/directional controller is based on roll angle, which is found from roll rate, the important control derivative for the autoland problem is $C_{l_{\delta_a}}$. The uncertainty in $C_{l_{\delta_a}}$ was arbitrarily chosen to be 25%.

The state-space form of the linearized longitudinal equations of motion are shown

Table II. Lateral/Directional Stability Derivative Uncertainty

Derivative	Importance	Accuracy
C_{y_β}	7	$\pm 20\%$
C_{l_β}	10	20
C_{n_β}	10	15
C_{y_p}	4	50
C_{l_p}	10	15
C_{n_p}	8	90
C_{y_r}	4	30
C_{l_r}	7	40
C_{n_r}	9	25

in (3.15).

$$\begin{bmatrix} 1 & -X_{\dot{\alpha}} & 0 & 0 \\ 0 & 1-\frac{Z_{\dot{\alpha}}}{U_1} & 0 & 0 \\ 0 & -M_{\dot{\alpha}} & 1 & 0 \\ 0 & 0 & 0 & 1 \end{bmatrix} \begin{bmatrix} \dot{u} \\ \dot{\alpha} \\ \dot{q} \\ \dot{\theta} \end{bmatrix} = \begin{bmatrix} X_u + X_{T_u} & X_\alpha & X_q & -gcos(\theta_1) \\ \frac{Z_u}{U_1} & \frac{Z_\alpha}{U_1} & \frac{Z_q}{U_1}+1 & -\frac{gsin(\theta_1)}{U_1} \\ M_u + M_{T_u} & M_\alpha + M_{T_\alpha} & M_q & 0 \\ 0 & 0 & 1 & 0 \end{bmatrix} \begin{bmatrix} u \\ \alpha \\ q \\ \theta \end{bmatrix} + \begin{bmatrix} \frac{X_{\delta_e}}{U_1} & \frac{X_{\delta_T}}{U_1} \\ Z_{\delta_e} & Z_{\delta_T} \\ M_{\delta_e} & M_{\delta_T} \\ 0 & 0 \end{bmatrix} \begin{bmatrix} \delta_e \\ \delta_T \end{bmatrix} \tag{3.15}$$

The parameters in (3.15) such as M_α and M_{δ_e} are functions of non-dimensional stability derivatives; e.g. M_α is a function of C_{m_α}, and M_{δ_e} is a function of $C_{m_{\delta_e}}$. Table III from Reference [28] displays the relative importance of each longitudinal derivative

and the accuracy to which it can be estimated using preliminary methods [29].

Table III. Longitudinal Stability Derivative Uncertainty

Derivative	Importance	Accuracy
C_{L_α}	10	$\pm 5\%$
C_{m_α}	10	10
C_{D_α}	5	10
C_{L_u}	4	20
C_{m_u}	7	20
C_{D_u}	1	20
C_{L_q}	3	20
C_{m_q}	9	20
C_{D_q}	1	20

Ground effect primarily affects C_{L_α}, and since the method for including ground effect is approximate, the uncertainty on C_{L_α} is increased to $\pm 25\%$. Because data does not exist for the control derivatives as mentioned above, the uncertainty values for the control derivatives are arbitrarily chosen. Since the throttle primarily controls airspeed, 25% uncertainty is added to $C_{D_{\delta_T}}$, and 25% uncertainty is added to $C_{m_{\delta_e}}$ because elevator is used to control pitch rate.

CHAPTER IV

DIGITAL CONTROLLER SYNTHESIS

This chapter describes the development of a digital QFT controller, which is used for comparison with a digital PI controller to control the aircraft during approach and landing. The control laws developed in this chapter will work with any guidance system as long as it provides precision approach data to the start of the flare. Both controllers are designed using a Single Input Single Output (SISO) model, but simulated using a Multiple Input Multiple Output (MIMO) system. By using the full model in simulation, all of the system dynamics are included. Each control law loop is designed independently and refined as necessary to achieve the desired response, and each control law loop is laid out in detail in the Appendix. MATLAB/Simulink [30] is used for control law synthesis and analysis.

Both control law designs utilize direct digital design for a sampled-data system (discrete compensator to control a continuous plant). The first step is to determine a suitable sample frequency which will provide a good response, prevent aliasing, and be as small as possible, so as to not overload the processor. Since this controller will be implemented on a UAV with assumed limited instrumentation, it is desired to have a slow sampling frequency so the control laws doe not impose a large computational burden. The sampling frequency is determined from the Shannon Sampling Theorem, which states that the frequency content of a signal can be recovered from its samples if the sampling frequency is at least twice the Nyquist frequency of the signal. The Nyquist frequency is the critical frequency at which aliasing starts to occur and is found from a plot of the plant eigenvalues. Fig. 8 displays the lateral directional eigenvalues, which include a first order actuator with a 0.1 sec time constant. The lateral/directional eigenvalues are used because they lead to a higher Nyquist frequency

than the longitudinal eigenvalues.

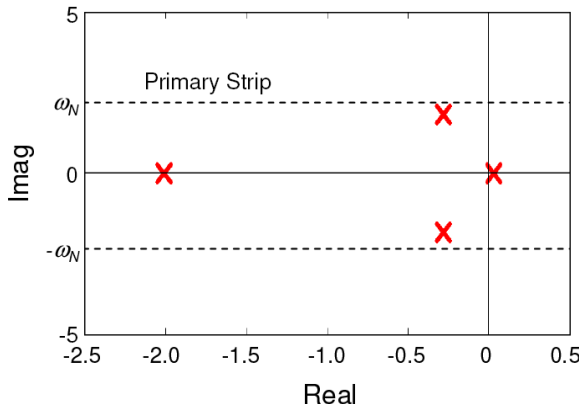

Fig. 8. Determination of Nyquist Frequency

By selecting the Nyquist frequency such that all eigenvalues of the system are contained within the primary strip, denoted by the dashed lines in the plot, aliasing can be prevented. From the figure, the Nyquist frequency was determined to be $\omega_N = 2$ rad/sec $= 0.31$ Hz, so the sampling frequency should be twice the Nyquist frequency, which is $\omega_s = 2\omega_N = 4$ rad/sec $= 0.62$ Hz. This sampling frequency is low for aircraft applications, and to recover amplitude content, the system must be sampled faster. To recover frequency and amplitude content and to ensure good performance of the controller, the sample frequency was chosen to be $\omega_s = 10$ Hz, which corresponds to a sample period of $T = 0.1$ sec [31].

The model is discretized using the z-transform, $z = e^{sT}$, where s is the Laplace variable, and T is the sample period. Specifications for the control laws developed were determined from Reference [29] as well as the author's experience flight testing autopilots. Ramp inputs were given to avoid excessive control surface positions and rates, and control positions and rates were limited by the chosen gains to be less than ± 10 deg and ± 15 deg/sec, respectively. The control laws should meet the

requirements specified in MIL-F-9490D [32], which gives the controller requirements as well as specifying a gain margin of at least 6 dB and a phase margin of at least 45 deg for all control loops. It is assumed that moderate turbulence will be the worst turbulence encountered, so the control laws are designed to be performance robust up to moderate turbulence. To evaluate the robustness of each loop, a singular value plot is used with singular values plotted in solid blue lines and frequency boundaries plotted in dashed red lines. It is desired for the singular values plot to be above the low frequency boundary, but below the high frequency boundary. The low frequency specifications are defined as follows [33]:

- Large minimum singular value
- Attenuation of low frequency disturbances by a factor of 0.25
- Slope of at least -20 dB/decade
- Zero steady-state error
- Minimum crossover frequency of 0.1 rad/sec
- Maximum crossover frequency of 10 rad/sec

The high frequency specifications are defined to be:

- Small maximum singular value
- Linear model accuracy to within $\pm 10\%$ of actual plant for frequencies up to 2 rad/sec, where uncertainty grows without bound at 20 dB/decade thereafter:

$$m(\omega) = \frac{s+2}{20} \tag{4.1}$$

where $m(\omega)$ is the multiplicative modeling discrepancy bound.

Fig. 9 illustrates the general control law structure, with the actuator and vehicle blocks replaced by inner-loops for sequential loop closures. The switches before and after the controller represent the sampling of the signals, which use a zero-order hold. Detailed control law diagrams are shown in the appendix for both the QFT and PI controllers.

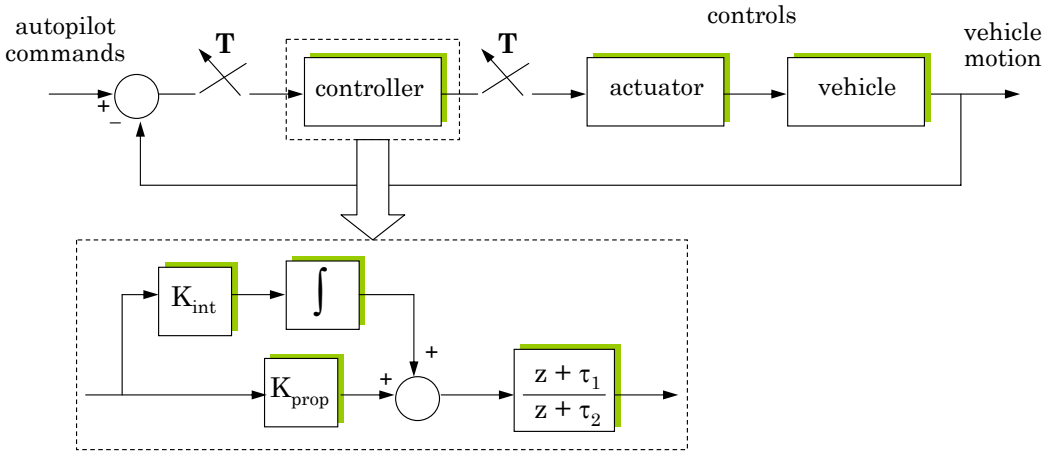

Fig. 9. Control Law Structure

A. Quantitative Feedback Theory Controller

Quantitative Feedback Theory is a robust control design technique that uses feedback to achieve responses that meet specifications despite structured plant uncertainty and plant disturbances. This technique has been applied to many classes of problems such as SISO, Multiple Input Single Output (MISO), and MIMO for both continuous and discrete cases. For this research, a SISO system is assumed for control law design, and sequential loop closures are utilized as with the proportional-integral controller. Consider the block diagram of Fig. 10. The objective of this design technique is to

synthesize $G(z)$ and $F(z)$, such that the output, y, satisfies the desired performance specifications for a reference input, r, for all plants in the set $\boldsymbol{P}$.

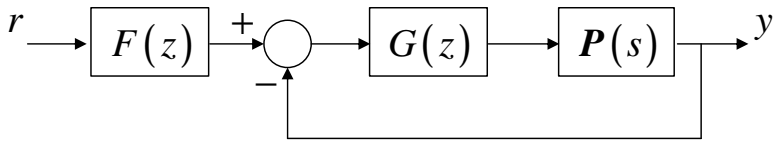

Fig. 10. QFT Block Diagram

The QFT design procedure can be summarized as follows:

1. Determine the set of plants, $\boldsymbol{P}$, which cover the range of structured parameter uncertainty as well as plant templates for each frequency of interest.
2. Specify acceptable tracking models, which the closed-loop response satisfies, $T_{R_L} \leq T_R \leq T_{R_U}$, and determine tracking bounds.
3. Determine disturbance rejection models, T_D, based on disturbance rejection specifications, and determine disturbance bounds.
4. Specify stability margin and determine U-contours.
5. Draw U-contours, disturbance bounds, and tracking bounds on a Nichols chart.
6. Synthesize nominal loop transfer function, $L_0(z)$.
7. Synthesize pre-filter, $F(z)$.
8. Simulate system to ensure performance meets specifications [14].

Using the list above as a guideline, each loop of the automatic flare system is designed using the QFT technique. When using sequential loop closure with QFT, most of the uncertainty lies in the inner-loops of the system, and after a suitable controller

is designed, outer-loops are subject to the same amount or less uncertainty. The design details of the outer-loops are not described in as much detail as the inner-loops because the procedure is similar for all loops. The Terasoft QFT Toolbox in MATLAB [34] is used for creating bounds and designing the control laws.

1. Lateral/Directional Controller

Design of the lateral/directional approach control laws involves three sequential loop closures. The innermost loop is bank angle command and hold followed by a heading hold and command loop, which is followed by a localizer tracker loop. Since the handling qualities of this aircraft are open-loop Level I for roll and Dutch roll modes, a roll damper and yaw damper are not designed. The bank angle command and hold serves as the inner-loop for the lateral/directional controller. The set of plants that cover the range of structured parametric uncertainty was determined using the analysis on model uncertainties in Chapter III. The nominal plant is chosen as the original model found using OKID without any errors included. The plant templates were determined by plotting the frequency response of every possible combination of stability and control derivative uncertainties, and using the boundary of these responses. Six frequencies were used for the design, $\omega = [0.1, 0.5, 2, 5, 15, 30]$ rad/sec. The templates obtained using these different frequencies are plotted in Fig. 11.

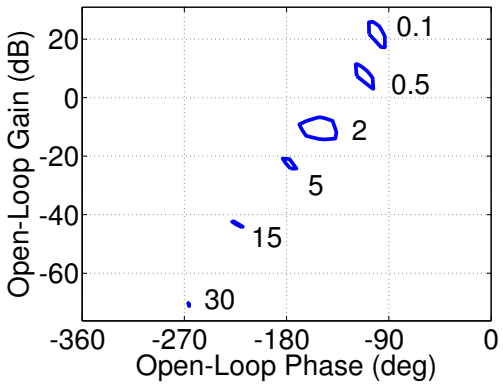

Fig. 11. Bank Angle Command and Hold Templates

The tracking models were determined using a set of specifications based on a unit step response. The rise time should be between 3 sec and 5 sec, and the overshoot should be less than 20%. Using this criteria, the transfer functions for T_{R_L} and T_{R_U} were determined to be as presented in (4.2).

$$T_{R_L} = \frac{1.25}{s^2 + s + 0.25} \tag{4.2a}$$

$$T_{R_U} = \frac{0.6944}{s^2 + 0.7599s + 0.6944} \tag{4.2b}$$

To help with the design of the pre-filter, it is common to add a pole to the lower tracking model and a zero to the upper tracking model, which do not affect the time history responses but increases the separation between the upper and lower models on a Bode magnitude plot as frequency increases [14]. (4.3) displays the resulting tracking models after adding the additional pole and zero. Fig. 12 shows the time response of the upper and lower tracking models as well as a Bode magnitude plot for the original models and the augmented models. The original models are plotted as blue dashed lines and the augmented models are plotted as red solid lines. As seen from the figure, the augmentation does not significantly affect the time response or the

desired specifications, but it does cause the separation between the Bode magnitude plots to increase as frequency is increased.

$$T_{R_L} = \frac{1.25}{s^3 + 6s^2 + 5.25s + 1.25} \tag{4.3a}$$

$$T_{R_U} = \frac{0.1389s + 0.6944}{s^2 + 0.7599s + 0.6944} \tag{4.3b}$$

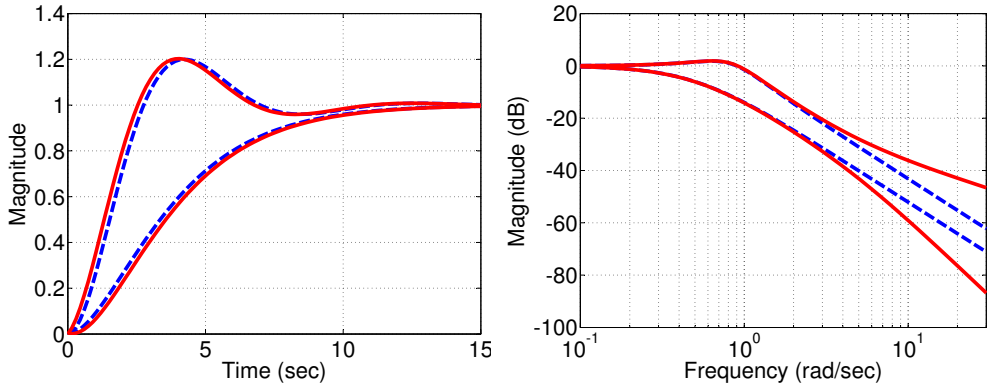

Fig. 12. Bank Angle Command and Hold Tracking Models

For this design, disturbance rejection will not be included because it was found that including disturbance rejection requirements results in large gains that exceed control position and rate limits. It was found that adequate disturbance rejection is provided by meeting the tracking requirements. The stability margin is determined based on the desired gain margin and phase margin for all plants in the set $\boldsymbol{P}$. For this problem a stability margin of 1.2 was used, which leads to $GM = 5.3$ dB and $PM = 49.3$ deg using (4.4).

$$GM = 20\log(1 + \frac{1}{SM}) \tag{4.4a}$$

$$PM = 180 - \cos^{-1}(\frac{0.1}{SM^2} - 1) \tag{4.4b}$$

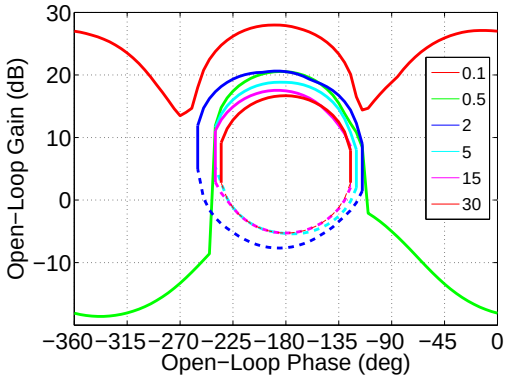

Fig. 13. Bank Angle Command and Hold Bounds

Using the QFT toolbox, the bounds and stability margins are plotted on a Nichols chart for each frequency value as in Fig. 13. Using these bounds, the nominal loop transfer function, L_0 should pass below and to the right of the oval bounds (stability bounds) and should be above the line bounds (tracking bounds) at that specific frequency. Fig. 14 portrays the nominal loop transfer function with and without the controller of (4.5).

$$G(z) = \frac{1.0369(z - 0.8484)}{(z - 0.8021)} \tag{4.5}$$

As seen in Fig. 14, the controller $G(z)$ is able to meet the specifications. The design of the pre-filter involves shaping the loop transfer function Bode magnitude plot such that the minimum and maximum responses lie within the tracking bounds. (4.6) displays the pre-filter as designed for the bank angle command and hold loop, and Fig. 15 shows the loop transfer function Bode magnitude plot with and without the

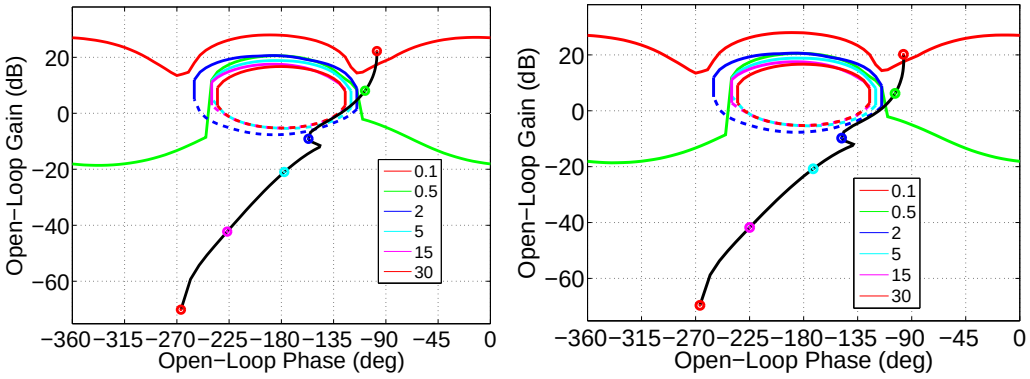

(a) Without Controller (b) With Controller

Fig. 14. Bank Angle Command and Hold Controller Synthesis

pre-filter, with the dotted lines representing the tracking bounds and the solid lines representing the minimum and maximum responses.

$$F(z) = \frac{0.23834(z^2 - 1.692z + 0.7331)}{(z^2 - 1.853z + 0.8633)} \tag{4.6}$$

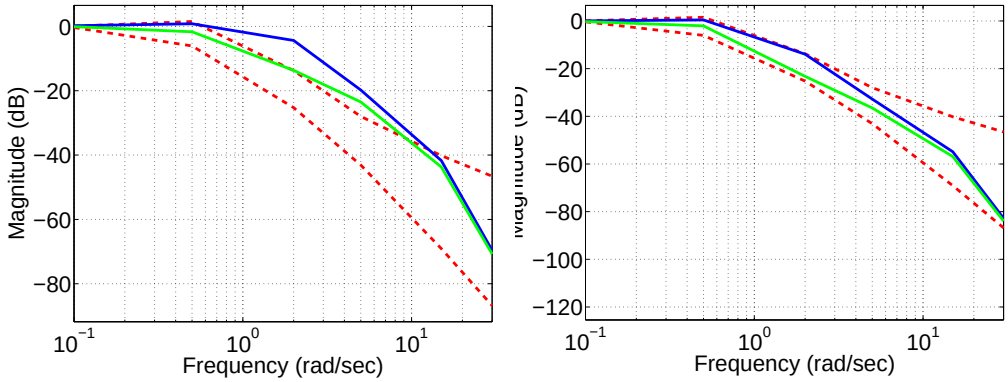

(a) Without Pre-Filter (b) With Pre-Filter

Fig. 15. Bank Angle Command and Hold Pre-Filter Synthesis

To validate the controller and pre-filter, the response to a step input is presented in Fig. 16 as well as a Bode magnitude plot to show that $G(z)$ and $F(z)$ meet the specifications for all plants in $\boldsymbol{P}$. As seen in the figure some of the responses do not

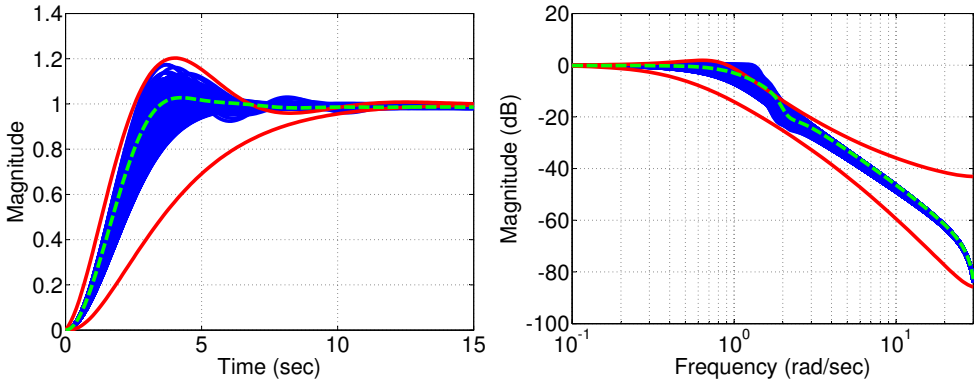

Fig. 16. Bank Angle Command and Hold Responses

meet the specifications, but it is assumed that the controllers are adequate. The solid red lines represent the tracking bounds, the solid blue lines are the response of each transfer function in the set $\boldsymbol{P}$, and the dashed green line shows the response of the nominal loop transfer function.

Using the closed-loop transfer functions from the bank angle command and hold loop, the heading command and hold loop was designed in a similar manner. A stability margin of 1.2 was used, and the tracking requirements were a rise time between 3 sec and 5 sec and an overshoot less than 10%. Using these specifications, the controller and pre-filter were designed as stated in (4.7).

$$G(z) = 0.902 \tag{4.7a}$$

$$F(z) = 1 \tag{4.7b}$$

Because of the robustness designed into the bank angle command and hold loop, the heading command and hold loop required only a single gain for adequate performance and robustness.

The localizer tracker is designed using the closed-loop heading command and hold

transfer functions as inner-loops. The desired localizer deviation is zero, making the reference input zero, thus designing a pre-filter is not necessary and tracking bounds are not included in the design. (4.8) presents the designed controller for the localizer tracker loop. As with the PI controller, the QFT localizer controller is scheduled with range to prevent the system from going unstable as the aircraft approaches the runway.

$$G(z) = \frac{0.001268(z - 0.9891)}{(z - 0.9766)} \tag{4.8}$$

To analyze the QFT controller, a singular values plot is used as in Fig. 17, with the low frequency and high frequency shown in dashed red lines, and the singular values response shown as a solid blue line. As seen from the figure, the localizer tracker does not meet the disturbance rejection requirement. The effect of not meeting this requirement will be analyzed further through simulations in Chapter VI.

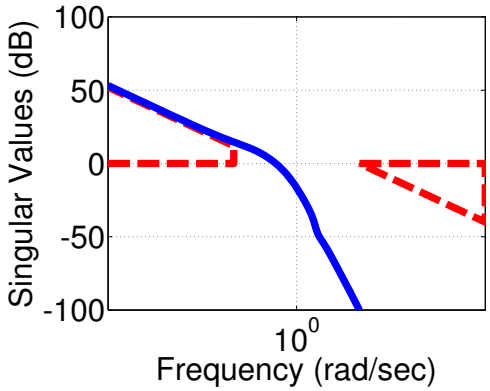

Fig. 17. QFT Localizer Tracker Singular Value Plot

2. Longitudinal Controller

The longitudinal controller consists of a glideslope tracker, automatic flare control law, and an airspeed command and hold control law. The glideslope tracker and autoflare loops are wrapped around the pitch angle command and hold loop. The airspeed command and hold loop involves a single loop closure, which contains the aircraft engine dynamics and throttle as the control. A description of the pitch angle command and hold loop is presented, followed by the design of the outer loops. Unlike the proportional-integral controller, the QFT design does not include a pitch damper because it was subsequently determined to be unnecessary for this design. The pitch angle command and hold loop will be used as the inner-loop for the glideslope tracker and the autoflare control loops. The airspeed command and hold loop will be designed independently of the pitch angle command and hold loop using the QFT technique.

A stability margin of 1.2 and tracking requirements of a rise time between 3 sec and 5 sec and an overshoot less than 20% were used for the controller synthesis. Using the QFT design technique as presented in the previous subsection, the pitch angle command and hold controller and pre-filter were designed as expressed in (4.9).

$$G(z) = \frac{0.85254(z - 0.9581)(z - 0.9546)}{(z - 1)(z - 0.7762)} \tag{4.9a}$$

$$F(z) = \frac{0.18902(z - 0.5434)}{(z - 0.9128)} \tag{4.9b}$$

Using the pitch command and hold loop as the inner-loop, the glideslope tracker is designed in a similar manner. Like the localizer tracker, the glideslope tracker is a regulator loop since it is desired for the glideslope deviation to approach zero. Tracking bounds and a pre-filter are not included in the design of the glideslope tracker since the reference input is zero, and the control laws are scheduled with

range to prevent instability in the system as the aircraft approaches the runway. The stability margin was chosen to be 1.2, leading to the same gain and phase margin as the pitch attitude command and hold loop. (4.10) presents the controller designed for the glideslope tracker.

$$G(z) = \frac{0.00264(z - 0.9899)(z - 0.9957)(z - 0.9826)}{(z - 1)(z - 0.9857)(z - 0.9772)} \tag{4.10}$$

It should be noted that some of the poles and zeros of the glideslope tracker are very close and could be canceled; however, these numbers are necessary to ensure the QFT stability and tracking bounds are met. Fig. 18 plots the singular values for the glideslope tracker. As seen in the figure, the controller developed for the glideslope tracker meets the requirements with the exception of the disturbance rejection requirement. The effect of not meeting the disturbance rejection specification will be evaluated further through simulation in Chapter VI.

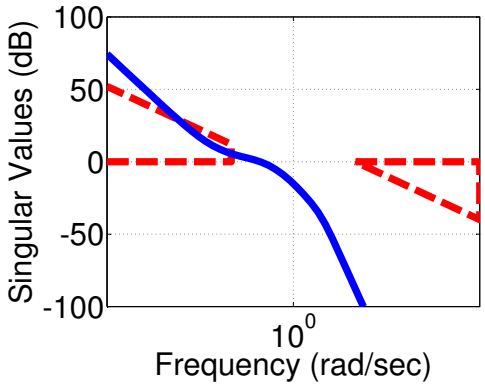

Fig. 18. QFT Glideslope Tracker Singular Values Plot

The automatic flare loop uses the same inner-loop as the glideslope tracker. Due to the presence of ground effect and the uncertainty associated with ground effect, a stability margin of 1.1 is used, which leads to a gain margin of 5.6 dB and a phase margin of 54.1 deg using (4.4). The tracking specifications for the autoflare loop were determined to be a rise time between 5 sec and 7 sec, and an overshoot less than 10%. Using the tracking bounds and stability bounds, the controller was designed to be as expressed in (4.11).

$$G(z) = \frac{0.0769(z - 0.9376)(z - 0.8733)}{z(z - 1)} \tag{4.11}$$

Fig. 19 displays the singular values plot for the automatic flare control loop and shows that the autoflare control law designed with QFT meets the specifications.

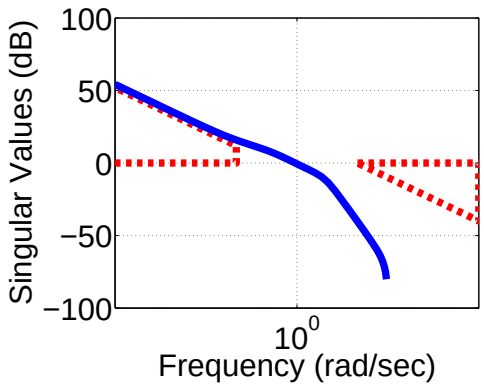

Fig. 19. QFT Automatic Flare Singular Values Plot

Airspeed command and hold is critical for the autoland system because it controls the speed of the aircraft during the approach and flare. If the airspeed becomes too low, the aircraft can stall and most likely lead to a crash due to the close proximity of the aircraft to the ground. If the airspeed is excessive, the aircraft could have problems tracking the glideslope and upon reaching the flare maneuver, the aircraft will either land at a speed too fast for landing or the aircraft will float down the runway and possibly run off the end of the runway. Airspeed control is obtained by regulating airspeed using throttle. The airspeed command and hold loop is designed in a similar manner as the pitch command and hold loop. A stability margin of 1.2 is used, and the tracking requirements are a rise time between 13 sec and 20 sec, and an overshoot less than 10%. Using the tracking bounds and stability bounds, the controller was designed as displayed in (4.12). A pre-filter was not needed for the airspeed command and hold loop.

$$G(z) = \frac{3.988(z - 0.972)(z - 0.938)}{(z - 1)(z - 0.7803)} \tag{4.12}$$

Using the designed controller, the closed-loop gain margin was found to be 27.9 dB and the closed-loop phase margin was found to be 98.7 deg, both of which meet the specifications. In summary, the QFT controller will provide adequate performance and robustness for approach and landing.

B. Proportional-Integral Controller

After discretizing the system, z-plane root locus is used to design the PI controller. Control law design for the system is accomplished through sequential loop closures. Proportional-Integral control uses proportional gain to improve response time and integral gain to reduce steady-state error. Because the PI controller is a SISO con-

troller and z-plane root locus is a SISO design tool, transfer functions were extracted for the various loops from the state-space models described in Chapter III.

1. Lateral/Directional Controller

The PI lateral/directional controller has the same structure as the QFT lateral/directional controller. Using z-plane root locus and sequential loop closure, the bank angle command and hold loop was designed using a proportional gain of 0.6, which leads to a gain margin (GM) of 27.6 dB and a phase margin (PM) of 67.4 deg. Using a proportional gain of 1.1, the heading command and hold loop was designed with a $GM = 15.3$ dB and $PM = 68.2$ deg. Plots of these inner-loops are not shown because the response of these loops will appear in the localizer tracker time histories.

The localizer tracker control law was developed by closing a loop around the heading command and hold loop. Due to the geometry of the localizer, as the aircraft gets closer to the runway, the course deviation becomes more sensitive. To account for this sensitivity, the localizer tracker gain is scheduled with slant range from the transmitter to prevent the controller from becoming unstable during the approach. The scheduled gain was selected to be 0.0003 and the proportional gain is 1.0. Integral gain is not needed, except when crosswinds are present. The selected gains result in $GM = 43.5$ dB and $PM = 20.9$ deg. Although the phase margin is lower than the specifications, changing the gains results in poor performance, so the selected gains are used. The singular value plot of Fig. 20 shows that the closed-loop system meets the high frequency specifications, but does not meet the low frequency specifications since it crosses into the dashed region.

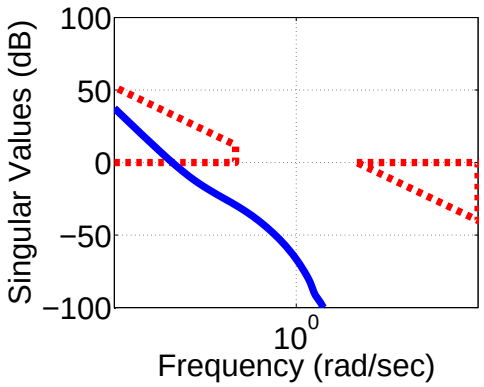

Fig. 20. PI Localizer Tracker Singular Values Plot

2. Longitudinal Controller

The longitudinal controller using the PI technique has the same form as the QFT controller, except the PI controller uses a pitch damper as the inner-most loop. The pitch damper was designed using a proportional gain of 0.164, which results in $GM =$ 28.4 dB and $PM = \infty$ deg. The pitch command and hold loop uses a proportional gain of 0.252 and a lead-lag filter with a lead constant of 0.983 and a lag constant of 0.0136. This controller leads to $GM = 33.1$ dB and $PM = 69.6$ deg. Similar to the geometry of the localizer tracker, the deviation becomes more sensitive as the aircraft approaches the transmitter, so the glideslope tracker gain is scheduled with slant range as the aircraft approaches the runway to prevent the system from becoming unstable. The glideslope scheduled gain was determined to be 0.003, the glideslope proportional gain was determined to be 1.0, and the glideslope integral gain was determined to be 0.01. These gains lead to $GM = 24.9$ dB and $PM = 8.62$ deg. The low phase margin is acceptable because the selected gains give good performance for the glideslope tracker. To evaluate the robustness of the glideslope control law developed, a singular values plot was constructed as presented in Fig. 21. This plot shows that the glideslope tracker satisfies the high frequency requirements, but not

the low frequency requirements. The selected gains provide good performance and will be used. The robustness will be analyzed further through simulations.

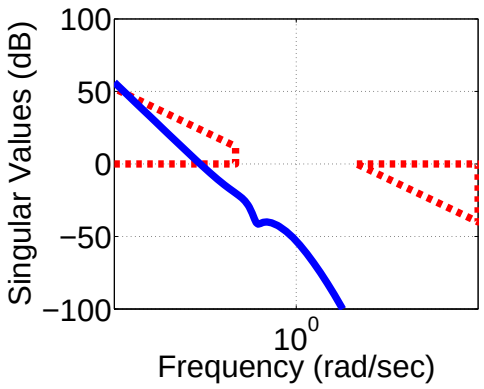

Fig. 21. PI Glideslope Tracker Singular Values Plot

The automatic flare control law wraps an additional loop around the pitch command and hold loop and is engaged upon reaching flare height. After the transition from the glideslope tracker controller to the automatic flare controller, the trajectory described in Chapter II is followed to the runway. Gains were selected using a z-plane root locus and were chosen to minimize touchdown velocity and range traveled during flare. The automatic flare controller uses proportional gain, which was chosen to be 7.0, and a lead-lag filter with a lead constant of 0.91 and a lag constant of 0.0697. The resulting gain margin is 18.7 dB, and the resulting phase margin is 69.7 deg. The singular values plot in Fig. 22 is used to analyze the robustness of the autoflare control law and shows that the autoflare control law meets both the low and high frequency specifications. As with the glideslope and localizer tracker loops, the robustness of the autoflare loop will be analyzed further through simulations.

Airspeed command and hold requires both rate and position feedback of the velocity. The proportional gain was chosen as 0.025, the integral gain was selected to be 1.0, the airspeed feedback gain was chosen to be 1.0, and the acceleration

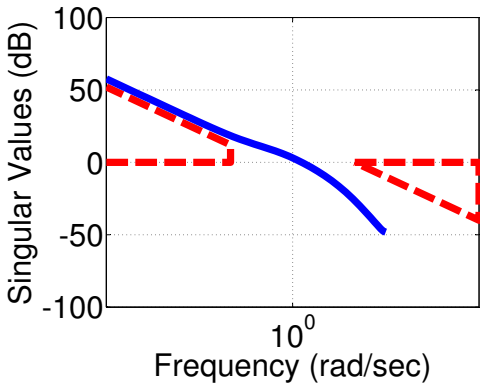

Fig. 22. PI Autoflare Singular Values Plot

feedback gain was chosen to be 5.0. The selected gains lead to a gain margin of 21.3 dB and a phase margin of 59.6 deg. The gains were selected such that the throttle position remains between idle (0%) and full power (100%) and a throttle rate of less than $\pm 10\%$/sec. In summary, a proportional-integral controller has been developed for approach and landing that provides good performance. The performance and robustness studies are presented in Chapter VI.

CHAPTER V

SELECTION OF APPROACH TYPES

This chapter presents various approach types that are considered to provide guidance accurate enough to be used for automatic landing. Three approach systems will be considered: Instrument Landing System (ILS), Microwave Landing System (MLS), and Global Positioning System (GPS).

A. Instrument Landing System

ILS is a ground based system which uses two transmitters to broadcast lateral and vertical guidance information. The lateral transmitter is known as the localizer, and the vertical transmitter is known as the glideslope. In addition to the localizer and glideslope, an ILS consists of marker beacons to provide range information along the approach path and approach lights to assist the pilot in seeing the runway. To use an ILS, each aircraft must be equipped with a localizer and glideslope receiver, a graphical display to show deviations, and marker beacon receivers. The localizer, glideslope, and marker beacon receivers are typically located on the vertical tail for general aviation aircraft, with the graphical display located in the cockpit.

Both the localizer and glideslope signals are subject to errors caused by various sources. A common source of errors is reflection caused by surface vehicles or even aircraft flying below 5,000 feet above the ground. Electromagnetic interference on the vehicle can also cause errors in the signals received. The errors associated with an ILS are typically low and do not significantly affect an aircraft's approach.

The localizer is a ground antenna array that broadcasts guidance data at 108.1 to 111.95 MHz. The structure is typically located on the extended runway centerline at the far end of the runway to prevent it from posing a collision hazard to aircraft.

The localizer coverage area extends from the transmitter to a distance of 18 NM and up to an altitude of 4500 feet above the elevation of the antenna site. A detailed drawing of the coverage area from Reference [22] is shown in Fig. 23.

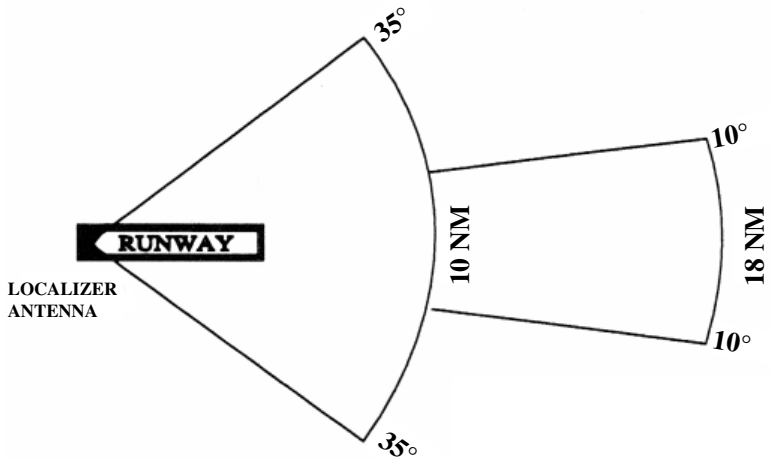

Fig. 23. Localizer Coverage Area

The localizer deviation is the angular difference between the aircraft position and the runway centerline. The localizer beam width is approximately five degrees, so full scale localizer deviation is 2.5 degrees. The narrowness of the localizer beam allows for an accurate approach to the runway centerline.

The glideslope transmitter is typically located approximately 750 to 1,250 feet from the runway threshold and between 400 and 600 feet to one side of the runway centerline, and uses the same type of signal as the localizer but at an angle between 2.5 degrees and 3.5 degrees above horizontal. The beam width of the glideslope is approximately 1.4 degrees and allows for precise control of the aircraft's altitude during the approach.

ILS approaches are divided into three categories based on the accuracy of the equipment used and weather requirements required to land after the approach. Each instrument approach has a minimum height to which the pilot can safely descend

using instruments in the cockpit. Once reaching the decision height, if the pilot cannot see the runway environment, the pilot must execute a missed approach. A category (CAT) I approach is the most common approach but is also the least accurate with a decision height of 200 feet. A CAT II approach allows for a decision height of 100 feet, and a CAT III approach does not have a decision height. CAT II and CAT III approaches require special ground equipment and automatic landing equipment aboard the aircraft [22].

A disadvantage of ILS is the limited availability. Of the approximately 197 airports with instrument approaches in the state of Texas, only 44 airports have an ILS approach and only 5 airports have a CAT III ILS approach as shown in Fig. 24. Despite the limited availability of CAT III ILS approaches, it remains the only approach approved by the FAA for automatic landing [35].

(a) Instrument Approaches (b) ILS Approaches (c) CAT III Approaches

Fig. 24. Texas Airports with Instrument Approaches

Reference [36] documents the required accuracies for aviation radio navigation systems, and the required accuracy for ILS systems is a localizer error of less than 0.06 deg and a glideslope error of 0.07 deg. For autopilot systems, the gain for both the localizer and glideslope is scheduled with range so the control laws do not drive the system unstable. Range is measured using Distance Measuring Equipment (DME).

DME is broadcast on the radio frequency used for an ILS and has an accuracy of 0.5 nm. This accuracy cited for DME is for a generic DME, not a DME associated with an ILS. Actual ILS DME accuracies are not known, so it is assumed that 0.5 nm is a conservative estimate of the DME accuracy [36].

B. Microwave Landing System

MLS was developed as a potential replacement for ILS and a few systems became operational in the late 1980s. MLS signals are transmitted in a frequency range of 5031 to 5091 MHz and provide azimuth, elevation, and range guidance information. Whereas the ILS signals are strictly aligned with the runway and at a fixed elevation angle, MLS permits pilot selection of approach azimuth and elevation angles from a single ground station. This ground station contains the azimuth, elevation, and range stations and can be placed anywhere on the airport, unlike ILS, which has specific installation requirements. The azimuth and elevation angles can range from ± 40 degrees and up to 15 degrees, respectively. This flexibility in azimuth angle allows for curved approaches to be possible [37]. Reference [38] documents flight test results of using MLS for automatic landing using both straight-in approaches and curved approaches, and the test results prove that MLS is capable to be used as approach for automatic landing. The accuracy of MLS is similar to that of ILS with the exception of the range accuracy. For ILS, the range is accurate to about 0.5 nm (3038.1 ft), and MLS is accurate to within 1600 ft [36]. About the same time MLS was being developed, GPS was starting to be developed and offered similar accuracy levels without expensive ground equipment at each airport. In 1994, the FAA suspended MLS research favoring the development of GPS. Due to limited GPS availability in Europe, MLS is being considered for widespread installation in Britain

and other parts of Europe.

C. Global Positioning System

GPS is a satellite based system which consists of three components to provide guidance: space, control, and user. The space component is a constellation of 24 Navstar satellites. These satellites are orbiting in six different orbital planes with four satellites in each plane at about 11,000 miles above the Earth. The constellation network broadcasts a pseudo-random code time signal and data message that can be processed to determine satellite position and status data. By triangulating between multiple satellites, the position of the aircraft can be determined. The control element consists of a ground-based network of monitoring and control stations that ensure the accuracy of satellite positions and clocks. Currently, there are five monitoring stations, three ground antennas, and a master control station. The user component consists of antennas and receivers on board the aircraft that provide positioning, velocity, and precise timing to the user. The aircraft GPS receiver measures distance from a satellite using the travel time of a radio signal. Each satellite transmits a specific code that contains information on the satellite's orbital position, system time, and the health and accuracy of the transmitted data. At least four satellites are needed for a three-dimensional position and time solution, and using a database of waypoints, the GPS receiver generates guidance information by comparing the aircraft's location to known waypoint locations [22].

GPS guidance for automatic landing is provided by comparing the aircraft's position to the runway's precise location and altitude. Position estimates are provided by GPS for latitude, longitude, and altitude. Since the latitude, longitude, and altitude are known for the runway, a trajectory can be generated for the aircraft to

follow until the flare height.

GPS is subject to errors due to loss of signals, electromagnetic interference, and atmospheric disturbances, although these errors are typically less than 50 feet, which allows this system to be used for instrument approaches. Although GPS is used for instrument approaches, the guidance information is not accurate enough for precision guidance or automatic landing; however, differential GPS (DGPS), the Wide Area Augmentation System (WAAS), and the Local Area Augmentation System (LAAS) offer corrections to GPS information that should provide guidance accurate enough for precision approaches in the near future.

DGPS was developed in the late 1980s and corrects GPS position estimates using ground stations to compare signals received from satellites with known positions on the ground. Reference [39] documents the flight test results of an automatic landing system using DGPS, and shows that 95% of the tested approaches provided guidance equal to that of conventional ILS guidance. The DGPS ground station corrections are valid only for that particular station location. As the distance from the station increases, the accuracy of DGPS decreases. At any given station, the DGPS error is between 0.5 m and 1.0 m and increases by 0.4 m for every 100 NM from the station. Even though the accuracy of DGPS increases with distance from a ground station, this system still provides accurate guidance capable for automatic landing [40].

Commissioned in 2003, WAAS works similar to DGPS to correct GPS signals, but unlike DGPS, the accuracy of WAAS is approximately uniform across the continental United States. Like DGPS, WAAS uses ground stations, approximately 25 across the US, to correct for disturbances in the ionosphere, which causes most of the errors in GPS position estimates. Two master stations on the east and west coast gather information from all 25 ground stations to create a correction to GPS estimates. This correction is broadcast to aircraft using two satellites. Broadcasting the signals over

satellites is a significant improvement over DGPS, which uses radio transmitters to broadcast correction information. By using satellites, the coverage area of the ground stations is increased and corrections are available to aircraft across the country [41].

LAAS is still in development and proposes to use ground stations located at an airport to provide local corrections to GPS signals. Because the corrections are for a limited area, the accuracy of the GPS signals with corrections would provide guidance to permit automatic landing guidance. Corrections are broadcast to nearby aircraft using VHF radio, similar to an ILS. A disadvantage of LAAS is that it requires ground equipment at each airport where it is to be used, but it proposes to provide performance similar to an ILS [42].

Even with the corrections that are available for GPS, currently the accuracy is only capable of an equivalent CAT I ILS. The FAA is continually working to increase the accuracy so that CAT II and CAT III operations can be possible in the near future. It appears that GPS with corrections will be the future and provide guidance capable of automatic landing. By using a correction that is not localized such as WAAS, automatic landing approach guidance is theoretically possible at most airports in the continental United States opening many more airports to automatic landing capability.

CHAPTER VI

NON REAL-TIME SIMULATION RESULTS

This chapter presents results from non real-time simulations, in which the objective is to evaluate the performance and performance robustness of the control laws developed in Chapter IV. These simulations are presented for the localizer, glideslope, and automatic flare control laws of the QFT controller and are compared to the PI controller. For this research "good" performance is assumed to be meeting the specifications for the nominal plant, and "good" performance robustness is assumed to be meeting the specifications with model uncertainties, turbulence, and sensor noise present.

For the test case, the aircraft is initially placed outside of the maximum deviation of the localizer on a heading that provides a 45 deg intercept angle, 6 nm from the runway, and flying straight and level at an altitude below the glideslope. The initial airspeed is the approach airspeed of 90 knots (151.90 ft/sec) and is maintained throughout the approach until reaching the flare height. After intercepting the localizer, the aircraft tracks the signal to the runway to remain aligned with the runway centerline. Upon intercepting the glideslope at a range of 4 nm, the aircraft descends and tracks the signal until the flare height. Upon reaching the flare height, the throttle is reduced and the flare maneuver is executed. A 6 nm localizer intercept and 4 nm glideslope intercept represents a worst case approaches since this is the closest to the runway that a localizer and glideslope interception would take place. These simulations assume the winds are aligned with the runway, which is justified by the fact that airplanes typically land into the wind. Crosswind landings are a daunting task for a controller and are beyond the scope of this research.

A summary of the controller simulation requirements are listed below, and each

value represents the 2σ number for each specification.

- Localizer cross distance, d_{cross}, less than 27 ft
- Glideslope altitude error, ALT_{error}, less than 5 ft
- Autoflare vertical speed at touchdown, VS_{TD}, greater than -6 ft/sec for soft landing and greater than -10 ft/sec for hard landing
- Autoflare flare distance traveled, d_{flare}, less than 1500 ft
- Autoflare aircraft speed at touchdown, V_{TD}, greater than stall speed (114.77 ft/sec)
- Autoflare aircraft pitch attitude angle, θ_{TD}, greater than -2 deg

A. Localizer Tracker Results

This section presents the simulation results for the localizer tracker. Nominal plant simulations are presented for both still and turbulence cases. Moderate turbulence is assumed to be the worst turbulence encountered. Monte Carlo simulations are presented for model uncertainties as defined by Chapter III, turbulence as defined in Reference [32], and sensor noise as defined by approach accuracies described in Chapter V.

1. Quantitative Feedback Theory Simulation

The QFT localizer tracker is simulated using the initial conditions described above. The nominal plant response of the localizer tracker is plotted for still and turbulent air cases in Fig. 25, which shows that the control laws successfully intercept and track the localizer without exceeding control positions or rates.

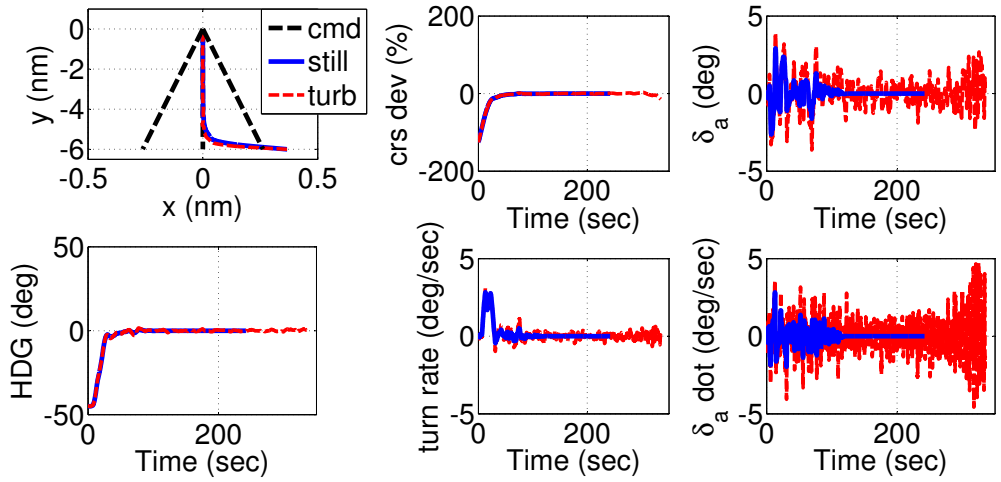

Fig. 25. QFT Localizer Tracker Performance Simulation

The results from the turbulence Monte Carlo simulation for the localizer are displayed in Fig. 26. Of the simulations conducted, 96.2% met the specifications for cross distance. The average cross distance was -1.33 ft with a standard deviation of 11.56 ft, which meets the specifications for localizer cross distance, indicating the localizer loop is robust to turbulence.

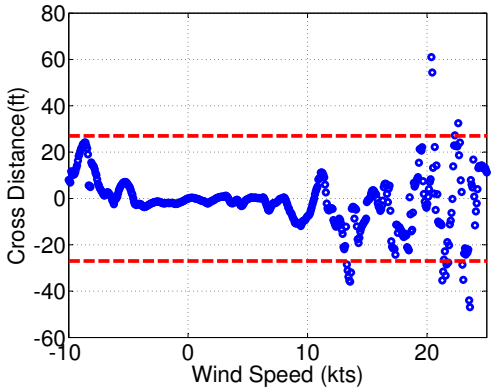

Fig. 26. QFT Localizer Tracker Turbulence Simulation

The model uncertainty Monte Carlo simulation results in a cross distance of less than 27 ft for all of the cases for still air with an average cross distance of 2.6e-4 ft

and a standard deviation of 1.6e-5 ft. When testing in turbulent air, the simulations show that 70% of the cases result in a cross distance less than 27 ft. The average cross distance was -15.4 ft and the standard deviation was 31.9 ft.

Using the accuracies described in Chapter V, sensor noise is added to the simulation for each approach discussed in Chapter V. It is assumed that an accurate system is aboard the aircraft to measure aircraft states, and errors in approach guidance will be the largest sensor errors. ILS and MLS errors are due to inaccuracies in the ground equipment, which leads to an angular error on the approach guidance. Due to the source of error, sensor noise is added to deviation values on the localizer and glideslope for ILS and azimuth and elevation for MLS. Errors when using GPS occur because of errors in position and altitude estimates. To simulate GPS sensor errors, noise is added to position and altitude used to determine horizontal and vertical deviations. To simulate sensor noise responses, 500 simulations are conducted for each approach type for still and turbulent air. Fig. 27 displays representative results from using ILS sensor noise.

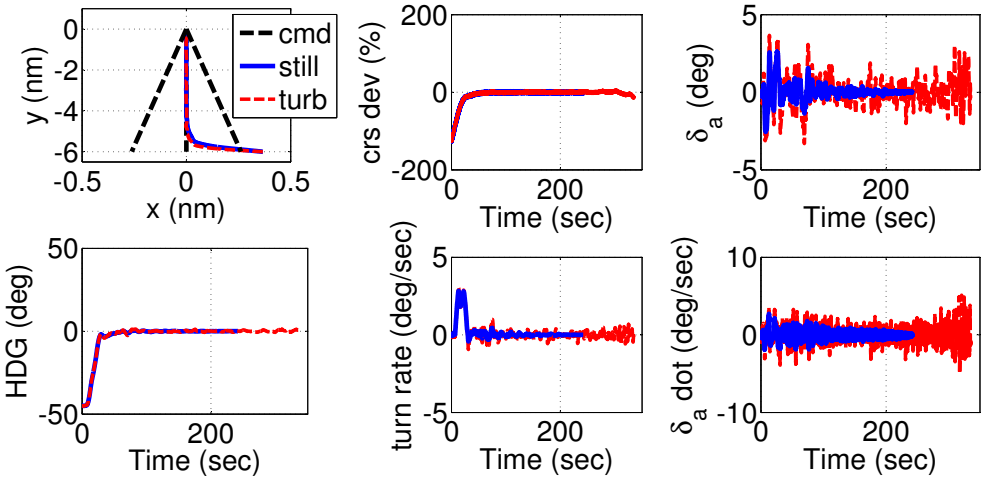

Fig. 27. QFT ILS Localizer Tracker Simulation

The QFT controller successfully guided the aircraft to within the specifications when using ILS sensor characteristics for all simulations in still air and 97.4% of the cases while in turbulence. The average cross distance for still air was 2.72 ft with a standard deviation of 0.358 ft, and while in turbulence, the average cross distance was found to be 0.957 ft with a standard deviation of 8.991 ft. Fig. 28 shows a representative simulation for an MLS approach.

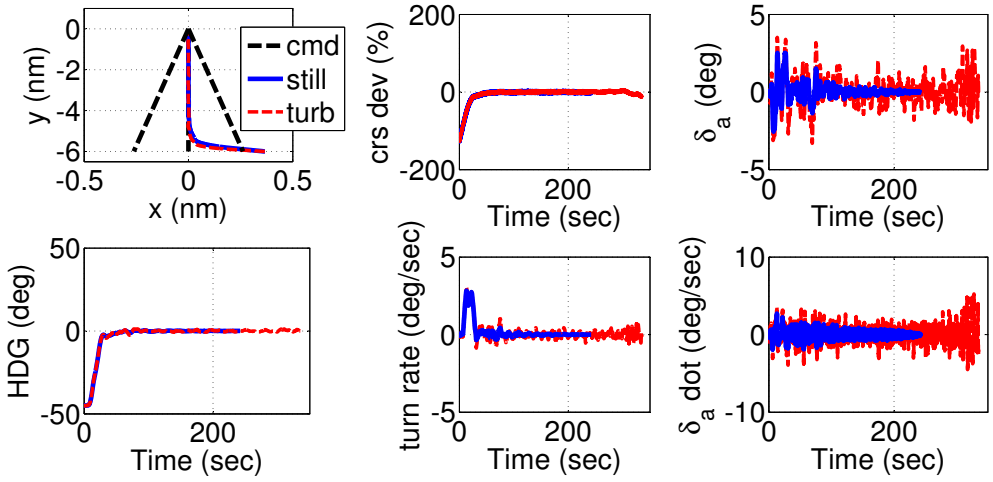

Fig. 28. QFT MLS Localizer Tracker Simulation

When using MLS sensor characteristics, the QFT controller resulted in successful approaches for each simulation conducted in still and turbulent air. The average cross distance was 1.41 ft with a standard deviation of 0.30 ft for still air, and for turbulent air the average cross distance was 0.75 ft with a standard deviation of 4.02 ft. Shown in Fig. 29 are two representative simulations for a GPS approach for still and turbulent air.

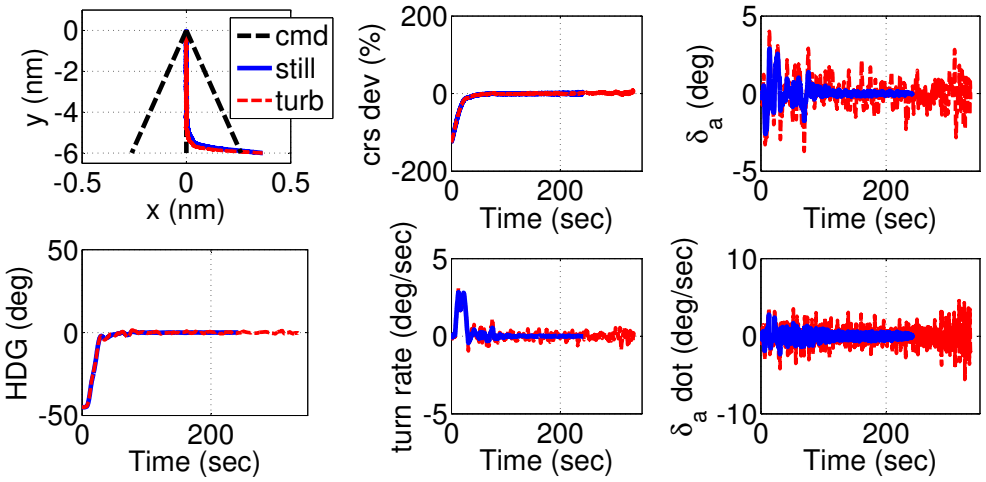

Fig. 29. QFT GPS Localizer Tracker Simulation

The GPS sensor characteristics resulted in successful approaches 100% of the time for both still air and turbulent air. In still air, the average cross distance was 0.37 ft with a standard deviation of 5.15 ft, and in turbulent air, the average cross distance was -5.23 ft with a standard deviation of 5.88 ft. Based on the approach sensor simulation results, it is concluded that the QFT controller is performance robust to sensor noise associated with ILS, MLS, and GPS approaches.

2. Proportional-Integral Simulation

The localizer tracker simulations are presented for only the outer-loop. Since this is the outermost loop, the inner-loop response characteristics are displayed through the outer-loop. Fig. 30 plots localizer time histories for the nominal plant for both still and turbulent air cases. As seen in the figure, the localizer intercepts and tracks to the runway with good performance for both the still and turbulent cases, while keeping the control position and rates within the specifications.

To test the performance robustness of the localizer tracker control laws, two Monte Carlo simulations are used. The first simulation tests the performance robust-

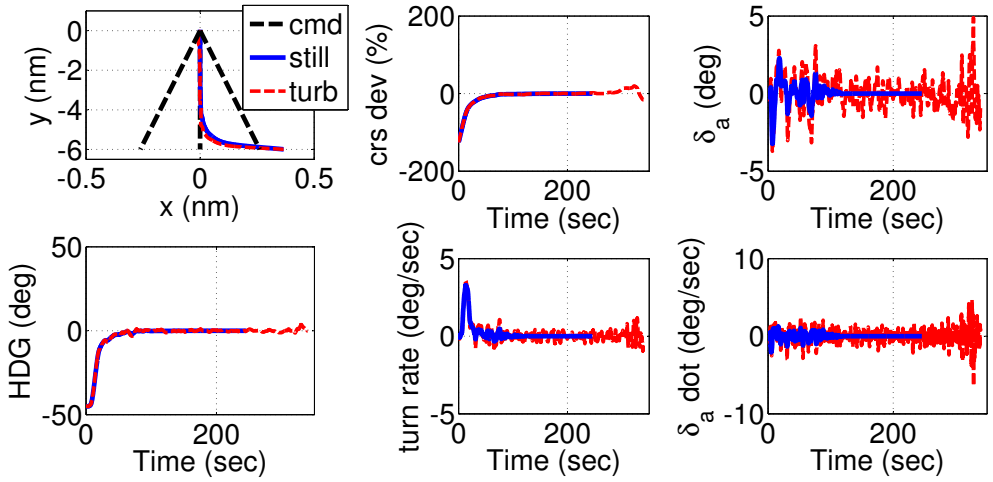

Fig. 30. PI Localizer Tracker Performance Simulation

ness of the controller to turbulence, and the second simulation tests the controller performance robustness to model uncertainties. To test the turbulence robustness of the localizer control laws, the nominal plant is simulated through a range of wind values starting at a 10 knot tailwind to a 25 knot headwind using a uniform distribution with 500 samples. A uniform distribution is used to cover the entire wind spectrum, and the 2σ cross distance from the runway centerline at touchdown should be less than 27 feet as defined in Reference [32]. Fig. 31 plots the cross distance at touchdown for each wind speed tested, and the dashed red lines show the cross distance required to meet the specifications of Reference [32]. From the simulations, the average cross distance is -4.35 ft with a standard deviation of 10.83 ft, which meets the specifications. Based on this simulation, it is concluded that the localizer control laws are robust to turbulence.

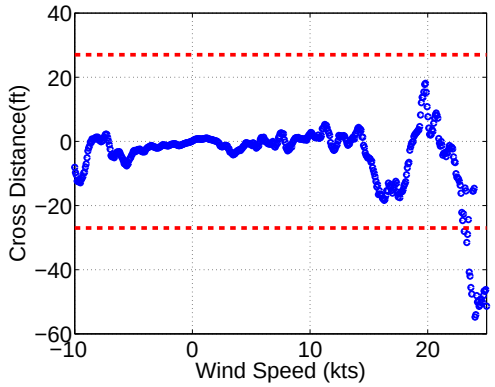

Fig. 31. PI Localizer Tracker Turbulence Simulation

Table IV lists the statistics from the turbulence Monte Carlo simulations for both the QFT and PI controllers, and it shows that both techniques exhibit performance robust to turbulence.

Table IV. Localizer Controller Turbulence Comparison

Performance Metric	QFT	PI
Percent Successful (%)	96.2	95.6
d_{cross} Average (ft)	-1.33	-4.35
d_{cross} Standard Deviation (ft)	11.05	10.83

The model uncertainty robustness is tested for still and turbulent air using the model uncertainties described in Chapter III. For the PI controller in still air, the PI controller successfully landed within 27 feet of the runway centerline for 100% of the cases. The average cross distance was found to be 0.212 ft with a standard deviation of 0.03 ft. To test the model uncertainty of the control laws in turbulent air, moderate turbulence is used in the same manner as for the nominal plant described above. During turbulent air cases, the PI control laws landed within the specifications 14% of the time, with an average cross distance of 0.62 ft and a standard deviation of 120.6

ft. From these results, the localizer PI controller is robust to model uncertainties in still air but not robust when moderate turbulence is present. Table V displays the statistics from the model uncertainty Monte Carlo simulations. When in still air, both controllers provide good performance robustness to model uncertainties, but in turbulent air, the QFT controller offers significantly better performance robustness than the PI controller.

Table V. Localizer Controller Model Uncertainty Comparison

Performance Metric	Still Air		Turbulence	
	QFT	PI	QFT	PI
Percent Successful (%)	100	100	69.8	14.0
d_{cross} Average (ft)	2.6e-4	0.21	-15.4	0.62
d_{cross} Standard Deviation (ft)	1.6e-5	0.03	31.9	120.6

The sensor noise Monte Carlo simulations for the PI controller use the same method and accuracies as used for the QFT controller. Fig. 32 displays representative results from using an ILS approach.

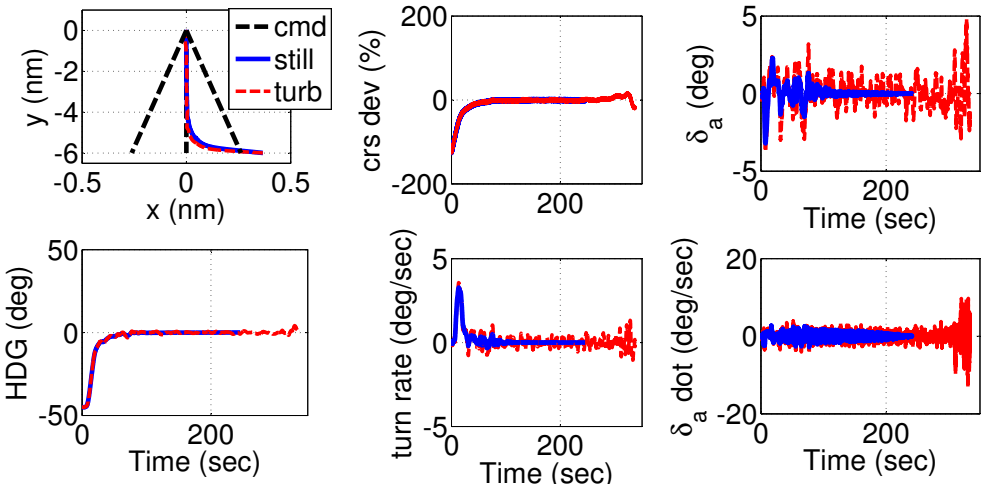

Fig. 32. PI ILS Localizer Tracker Simulation

With still air, the PI controller successfully guided the aircraft within the specifcations each time and with turbulence included, the PI controller was successful 60.4% of the cases. The average cross distance was 2.254 ft with a standard deviation of 0.168 ft for still air, and for turbulence, the average cross distance was -35.60 ft with a standard deviation of 1049.95 ft. Fig. 33 shows a representative simulation for an MLS approach.

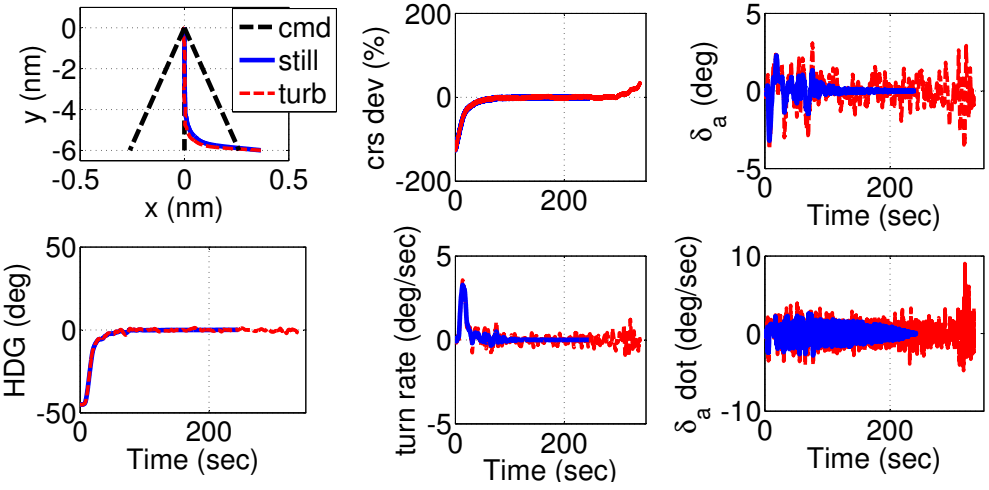

Fig. 33. PI MLS Localizer Tracker Simulation

The MLS simulations resulted in successful approaches 100% of the time for still air and 66.8% of the time for turbulent air. For still air, the average cross distance was 1.24 ft with a standard deviation of 0.19 ft, and the turbulence simulations resulted in an average cross distance of 10.12 ft and a standard deviation of 26.77 ft. Shown in Fig. 34 are two representative simulations for a GPS approach for still and turbulent air.

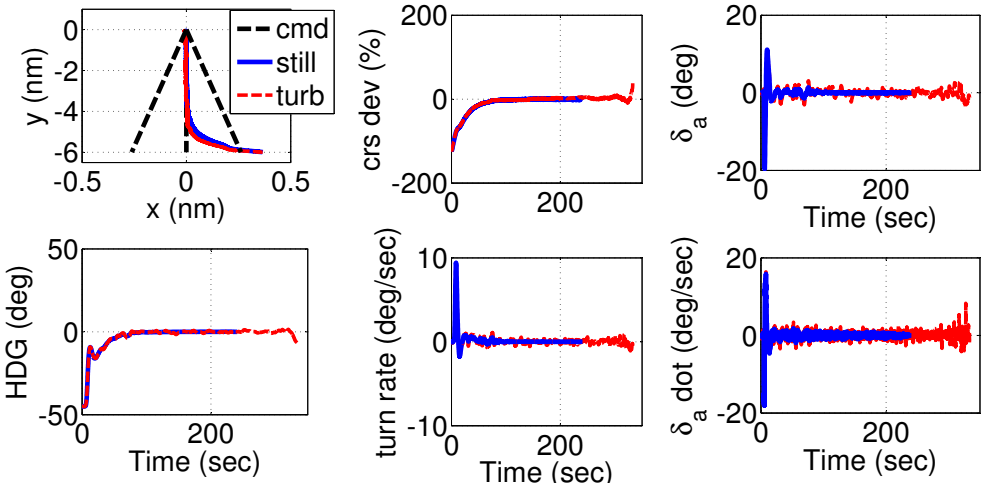

Fig. 34. PI GPS Localizer Tracker Simulation

The PI controller using GPS sensor characteristics resulted in all simulations in still air meeting the requirements, while 37.2% of the simulations met the specifications in turbulence. The average cross distance for still air was 0.41 ft with a standard deviations of 5.23 ft. In turbulence, the average cross distance was 0.031 ft with a standard deviation of 53.12 ft. Table VI through Table VIII summarize the localizer results for sensor noise Monte Carlo simulations for still air and turbulence for both QFT and PI controllers.

Table VI. Localizer ILS Sensor Comparison

Performance Metric	Still Air		Turbulence	
	QFT	PI	QFT	PI
Percent Successful (%)	100	100	97.4	60.4
d_{cross} Average (ft)	2.72	2.25	0.96	-35.60
d_{cross} Standard Deviation (ft)	0.36	0.17	8.99	1049.95

Table VII. Localizer MLS Sensor Comparison

Performance Metric	Still Air		Turbulence	
	QFT	PI	QFT	PI
Percent Successful (%)	100	100	100	66.8
d_{cross} Average (ft)	1.41	1.24	0.75	10.12
d_{cross} Standard Deviation (ft)	0.30	0.19	4.02	26.77

Based on the simulation results for sensor noise, the QFT and PI controllers both offer similar performance robustness in still air, but in turbulent air the QFT controller offers significantly better performance robustness.

Table VIII. Localizer GPS Sensor Comparison

Performance Metric	Still Air		Turbulence	
	QFT	PI	QFT	PI
Percent Successful (%)	100	100	100	37.2
d_{cross} Average (ft)	0.37	0.41	-5.23	0.03
d_{cross} Standard Deviation (ft)	5.15	5.23	5.88	53.12

B. Glideslope Tracker Results

The glideslope control law simulations are presented in this section, starting with the QFT controller followed by the PI controller. To evaluate the glideslope tracker, the aircraft is initially flying level, intercepts the glideslope 4 nm from the runway, and tracks it to the runway.

1. Quantitative Feedback Theory Simulation

For the QFT controller, Fig. 35 shows that the glideslope control laws provide good performance and meet the specifications for the nominal plant in still and turbulent air cases.

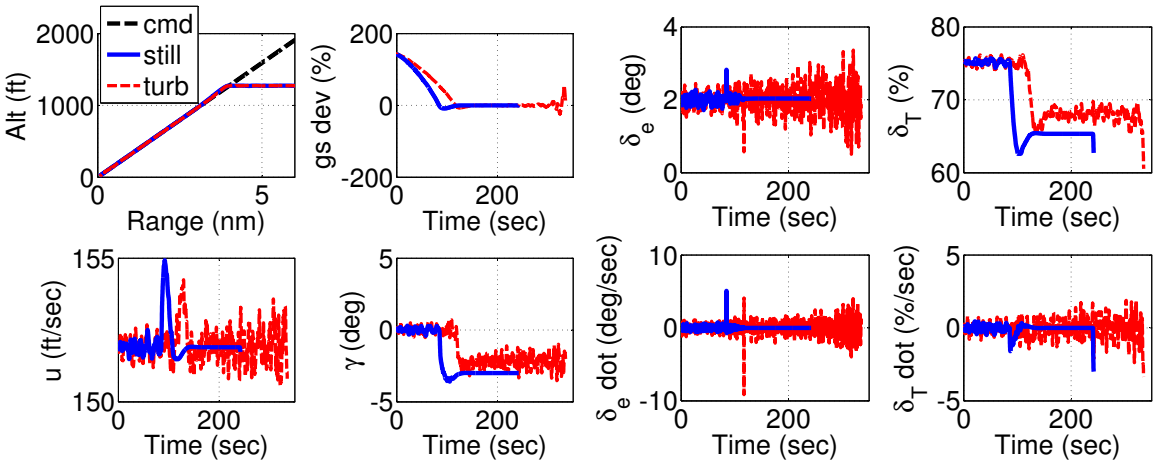

Fig. 35. QFT Glideslope Tracker Performance Simulation

Based on the turbulence Monte Carlo simulation results plotted in Fig. 36, the glideslope tracker meets the specifications for glideslope tracking 97% of the time with a mean altitude error of 0.96 ft and a standard deviation of 1.27 ft. These results show good performance robustness to turbulence for the nominal plant.

The model uncertainty simulations result in all of the cases in still air meet the 5

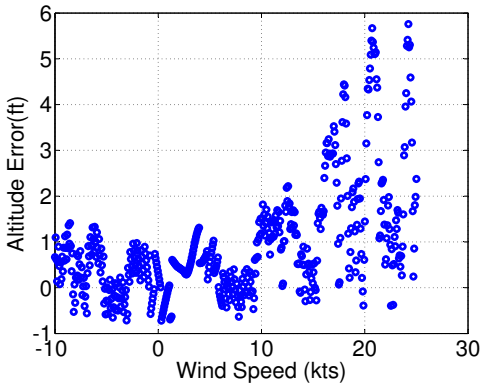

Fig. 36. QFT Glideslope Tracker Turbulence Simulation

ft altitude error specification with an average error of 0.1 ft and a standard deviation of 0.3 ft. When tested in turbulent air, the glideslope controller results in a successful approach to within 5 ft altitude error 80% of the time. The average altitude error was 2.7 ft with a standard deviation of 2.3 ft, showing a significant improvement over the PI controller. From these simulations, the glideslope controller provides good performance for the nominal plant, and exhibits good performance robustness to turbulence for the nominal plant as well as insensitivity to model uncertainties for still air. As the turbulence increases, the performance robustness to model uncertainty decreases but still provides an acceptable level of performance robustness.

The sensor noise Monte Carlo simulations for the PI controller use the same method and accuracies as used for the QFT controller, and Fig. 37 displays representative results from using an ILS approach.

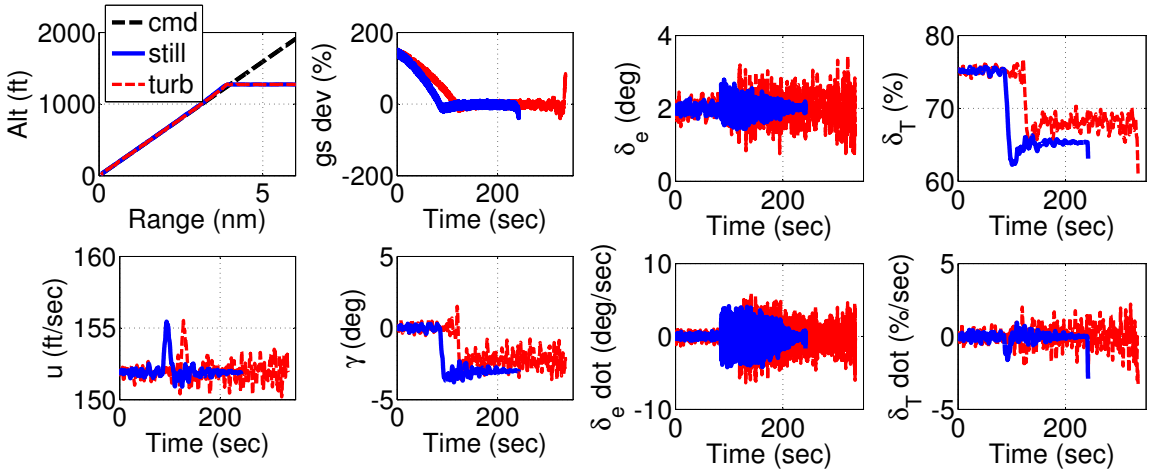

Fig. 37. QFT ILS Glideslope Tracker Simulation

Using the QFT controller with an ILS approach resulted in a successful approach 100% of the time in still air and 94.2% of the time for turbulent air. In still air, the average altitude error was 1.72 ft and the standard deviation was 0.40 ft. In turbulent air, the average altitude error was 2.14 ft and the standard deviation was 1.60 ft. Fig. 38 shows a representative simulation for an MLS approach.

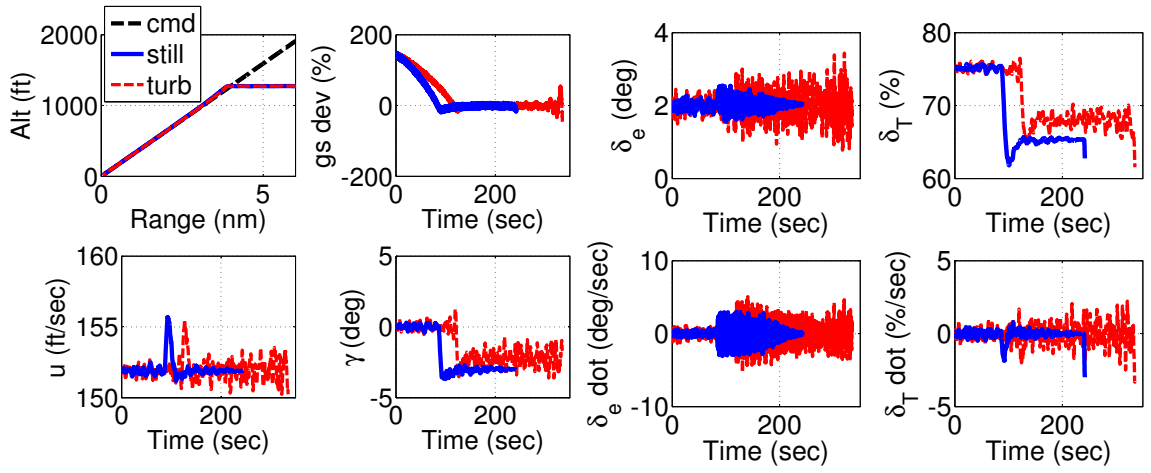

Fig. 38. QFT MLS Glideslope Tracker Simulation

When using MLS sensor characteristics, the QFT controller resulted in successful approaches 100% of the time for still air and 99.4% of the time for turbulent air. The average altitude error for still air was 0.96 ft with a standard deviation of 0.22 ft, and in turbulent air, the average altitude error was 1.91 ft with a standard deviation of 1.28 ft. Shown in Fig. 39 are two representative simulations for a GPS approach for still and turbulent air.

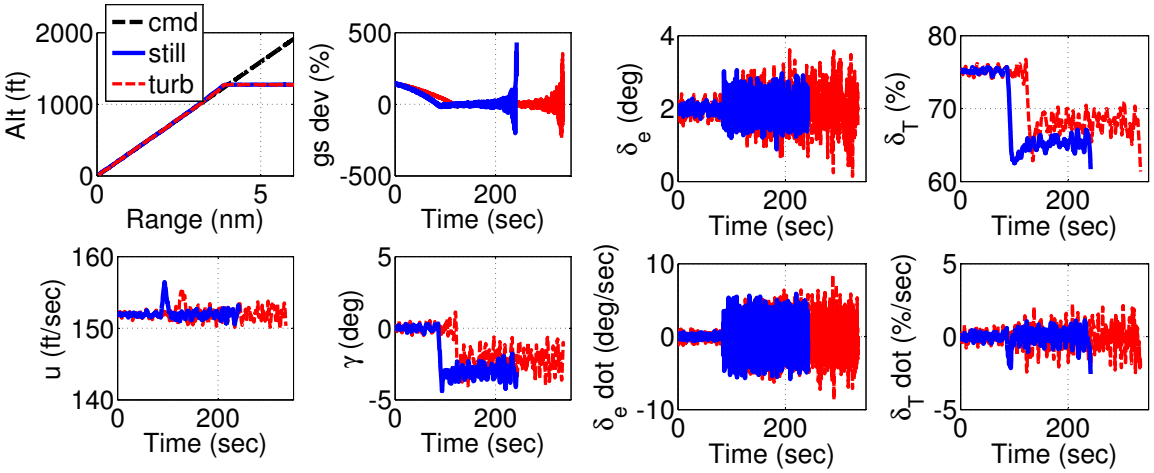

Fig. 39. QFT GPS Glideslope Tracker Simulation

The QFT controller resulted in 94% successful simulations for still air and 80.6% successful simualtions for turbulent air when using GPS sensor characteristics. The average altitude error in still air was 0.30 ft with a standard deviation of 2.68 ft, and in turbulent air the average altitude error was 0.80 ft with a standard deviation of 3.86 ft. The robustness of the GPS sensor characteristics is lower because of the large errors associated with estimating altitude using GPS. The lack of robustness is not a fault of the controller but a limitation in the current technology.

2. Proportional-Integral Simulation

The plots in Fig. 40 show the glideslope response for still and turbulent air cases using the nominal plant for the PI controller.

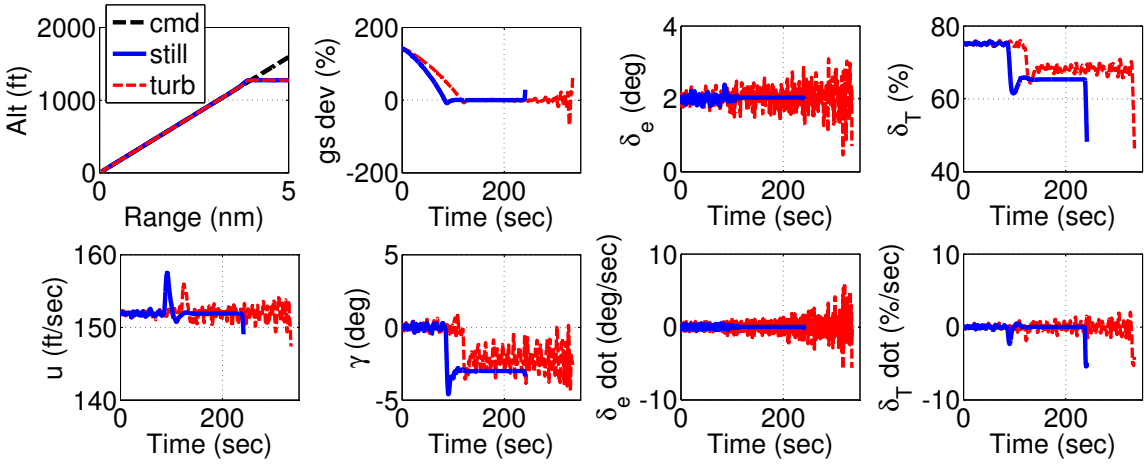

Fig. 40. PI Glideslope Tracker Performance Simulation

As seen in the plots, the glideslope tracker performs well for both the nominal case and the case with turbulence. To evaluate the performance robustness of the glideslope control law to turbulence, a Monte Carlo simulation was conducted with 500 simulations, and altitude error is plotted against wind speed as displayed in Fig. 41. The altitude error plotted is the difference between the altitude when the flare should start and the actual flare height. According to Reference [32], the glideslope control laws should maintain the aircraft within 12 feet of the glideslope centerline to a distance of 100 feet above the ground. Since the glideslope tracker is used to a distance of approximately 20 feet above the ground, the glideslope tracking requirement is decreased to a 2σ altitude error within ± 5 feet of the glideslope centerline. The turbulence robustness simulation results for the glideslope tracker are plotted in Fig. 41. As seen in the plot, the altitude error is less than one foot for all cases run, and the average altitude error was found to be 0.5 ft with a standard

deviation of 0.73 ft. This result shows excellent performance robustness to turbulence for the glideslope tracker using the nominal plant.

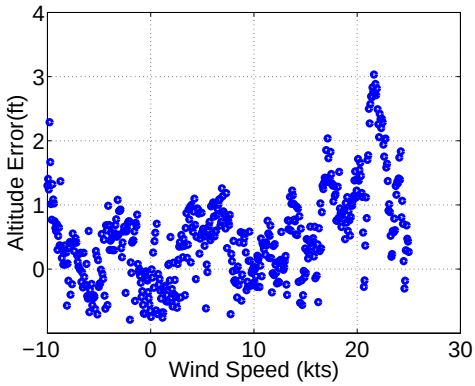

Fig. 41. PI Glideslope Tracker Turbulence Simulation

Table IX presents a comparison of the PI and QFT glideslope controllers for the turbulence Monte Carlo simulations. The results show that both controller types offer good performance robustness to turbulence for the nominal plant.

Table IX. Glideslope Controller Turbulence Comparison

Performance Metric	QFT	PI
Percent Successful (%)	97.4	100
ALT_{error} Average (ft)	0.96	0.5
ALT_{error} Standard Deviation (ft)	1.27	0.73

The model uncertainty robustness simulations result in a 100% success rate with an average altitude error of -0.211 ft and a standard deviation of 0.138 ft in still air. When tested with turbulent air, the glideslope control law resulted in a successful approach for 42% of the cases with an average altitude error of 8.3 ft and a standard deviation of 5.6 ft. Based on these simulations, the glideslope control law is robust to model uncertainties in still air but when turbulence is present, the controller is

not robust to model uncertainties. Results from the model uncertainty Monte Carlo simulations are displayed in Table X. The results show that both controllers are robust to model uncertainties when in still air, but in turbulent air, the QFT controller offers significantly better performance robustness to model uncertainties.

Table X. Glideslope Controller Model Uncertainty Comparison

Performance Metric	Still Air		Turbulence	
	QFT	PI	QFT	PI
Percent Successful (%)	100	100	80.4	41.7
ALT_{error} Average (ft)	0.098	-0.21	2.7	8.3
ALT_{error} Standard Deviation (ft)	0.30	0.14	2.3	5.6

The sensor noise Monte Carlo simulations for the PI controller use the same method and accuracies as used for the QFT controller. Fig. 42 displays representative results from using an ILS approach.

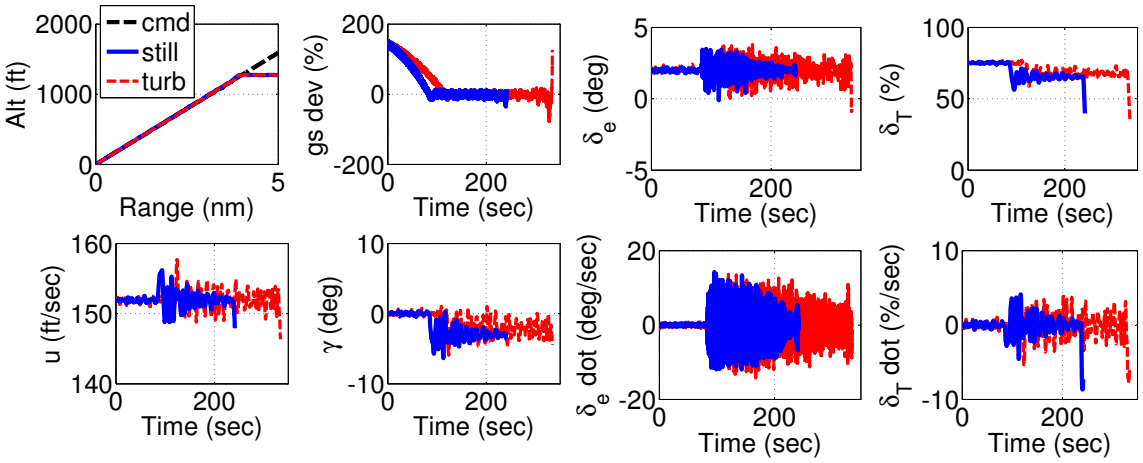

Fig. 42. PI ILS Glideslope Tracker Simulation

In still air, all of the simulations were successful with an average altitude error of 0.44 ft and a standard deviation of 0.54 ft. When simulated in turbulence, 53% of

the cases were successful. The average altitude error was 5.61 ft and the standard deviation was 4.18 ft. Fig. 43 shows a representative simulation for an MLS approach.

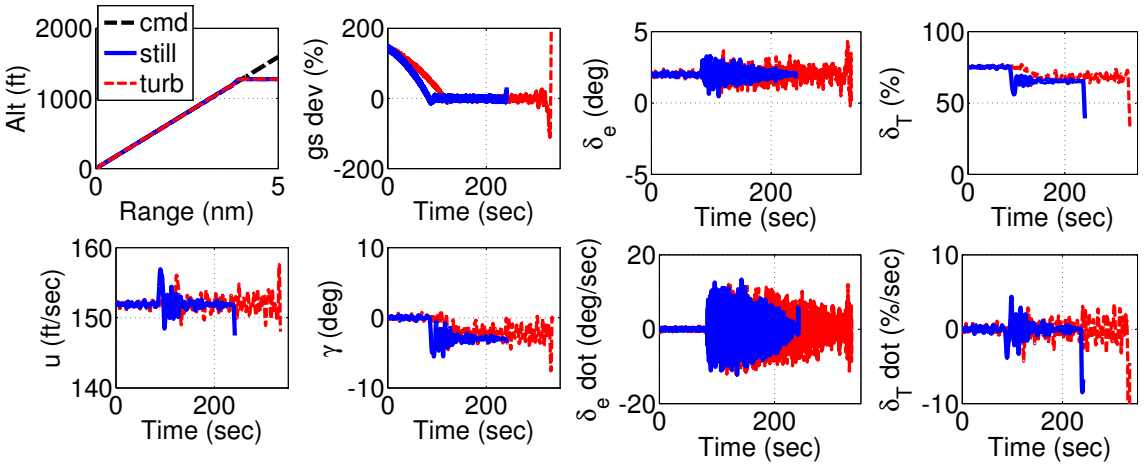

Fig. 43. PI MLS Glideslope Tracker Simulation

When using an MLS approach, 100% of the simulations conducted met the specifications with an average altitude error of 1.00 ft and a standard deviation of 0.34 ft. In turbulence, 57.2% of the simulations met the specifications with an average altitude error of 5.06 ft and a standard deviation of 3.16 ft. Shown in Fig. 44 are two representative simulations for a GPS approach for still and turbulent air.

In still air, 66.8% of the simulations met the requirements. The average altitude error was 0.95 ft with a standard deviation of 5.07 ft. In turbulence, 27.8% of the simulations were successful, and the average altitude error was 4.01 ft with a standard deviation of 8.84 ft. Table XI through Table XIII summarize the localizer results for sensor noise Monte Carlo simulations for still air and turbulence for both QFT and PI controllers.

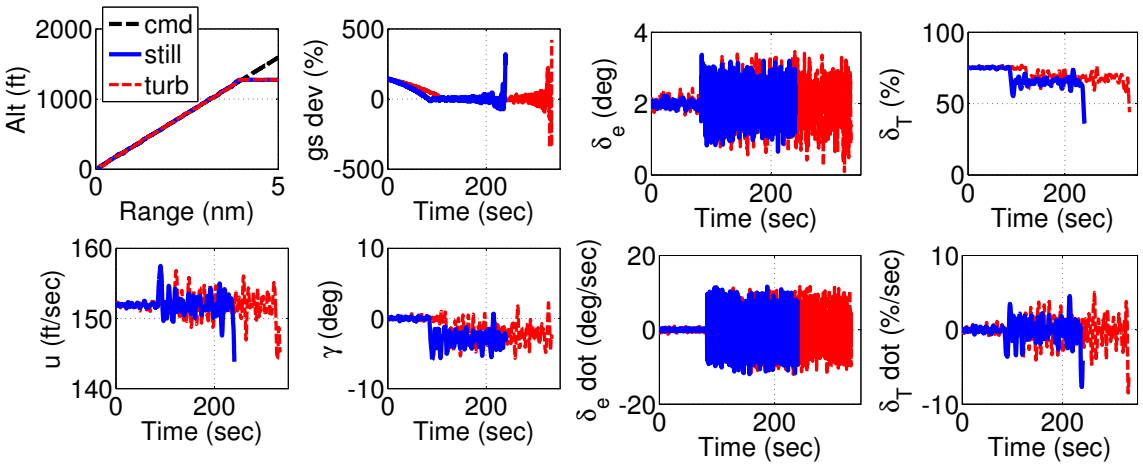

Fig. 44. PI GPS Glideslope Tracker Simulation

Table XI. Glideslope ILS Sensor Comparison

Performance Metric	Still Air		Turbulence	
	QFT	PI	QFT	PI
Percent Successful (%)	100	100	94.2	53.0
ALT_{error} Average (ft)	1.72	0.44	2.14	5.61
ALT_{error} Standard Deviation (ft)	0.40	0.54	1.60	4.18

As seen from the results of the sensor Monte Carlo simulations, the QFT and PI controllers offer similar performance robustness in still air, but in turbulent air, the QFT controller offers significantly better performance robustness.

C. Automatic Flare Controller Results

To simulate the autoflare control law, the aircraft tracks the glideslope to the flare height of 17.47 ft, and then the flare maneuver is executed. At the flare height, the airspeed is commanded to a value just above the stall speed of the aircraft, which is 68 knots (114.77 ft/sec) in the landing configuration.

Table XII. Glideslope MLS Sensor Comparison

Performance Metric	Still Air		Turbulence	
	QFT	PI	QFT	PI
Percent Successful (%)	100	100	99.4	57.2
ALT_{error} Average (ft)	0.96	1.00	1.91	5.06
ALT_{error} Standard Deviation (ft)	0.22	0.34	1.28	3.16

Table XIII. Glideslope GPS Sensor Comparison

Performance Metric	Still Air		Turbulence	
	QFT	PI	QFT	PI
Percent Successful (%)	94.0	66.8	80.6	27.8
ALT_{error} Average (ft)	0.30	0.95	0.80	4.01
ALT_{error} Standard Deviation (ft)	2.68	5.07	3.86	8.84

1. Quantitative Feedback Theory Simulation

The QFT automatic flare controller nominal plant simulations are presented in Fig. 45 for still and turbulent air. These plots show that the control laws for autoflare provide good performance and a smooth, safe touchdown for still and turbulent cases.

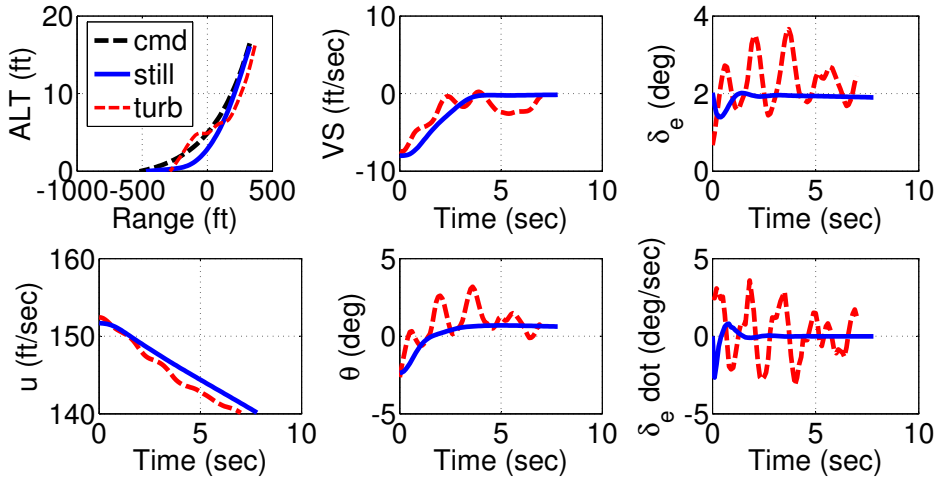

Fig. 45. QFT Automatic Flare Performance Simulation

The turbulence Monte Carlo simulations in Fig. 46 result in 99.6% soft landings and 0.4% hard landings. The average touchdown vertical velocity for the automatic flare was -0.52 ft/sec with a standard deviation of 0.91 ft/sec, and the average touchdown range was -669 ft with a standard deviation of 223 ft. The average pitch attitude angle was 0.1 deg with a standard deviation of 0.9 deg, and the average forward velocity was 141 ft/sec with a standard deviation of 2.6 ft/sec. Since the nominal plant meets the specifications for the Monte Carlo turbulence simulations, the automatic flare control laws are robust to turbulence for the nominal plant.

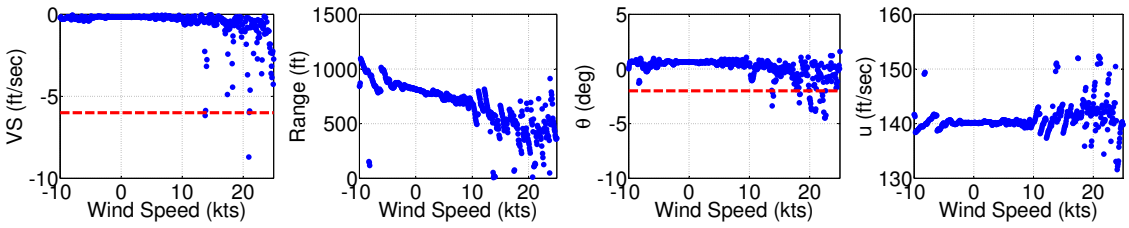

Fig. 46. QFT Automatic Flare Turbulence Simulation

The model uncertainty simulations show that the autoflare control laws success-

fully meet the specifications for all of the cases in still air. The average touchdown vertical velocity was -0.14 ft/sec with a standard deviation of 0.02 ft/sec. When turbulence is included, the simulations result in 97% soft landings, 1% hard landings, and 2% damage landings. The average touchdown vertical velocity was -0.52 ft/sec with a standard deviation of 0.99 ft/sec. This shows good performance robustness to model uncertainties, even in the presence of moderate turbulence.

2. Proportional-Integral Simulation

Fig. 47 presents time history responses of the autoflare nominal loop for still and turbulent cases for the PI controller.

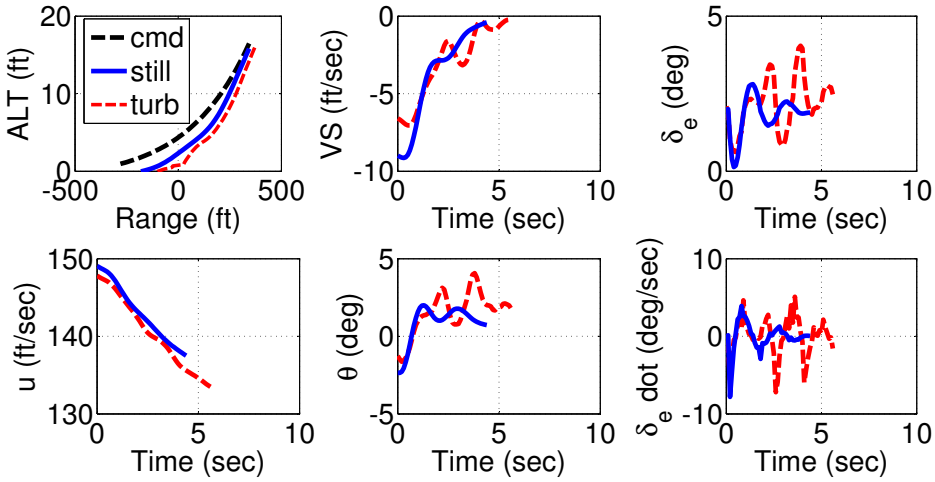

Fig. 47. PI Automatic Flare Performance Simulation

According to Reference [32], the distance the aircraft travels during the flare should be less than 1500 feet, and Reference [21] states that the vertical velocity at touchdown should be greater than -6 ft/sec for a smooth landing. A soft landing is considered to be a landing with a vertical speed between 0 ft/sec and -6 ft/sec, a hard landing is a landing with a vertical speed between -6 ft/sec and -10 ft/sec, and

a damage landing is a landing with a vertical speed less than -10 ft/sec. To prevent stalling before touchdown, the speed of the aircraft should be greater than the stall speed. The pitch attitude angle of the aircraft should be greater than the resting pitch attitude angle of the aircraft when the vehicle is resting on the ground, which for the aircraft used is -2 deg. For this research, each of the specifications above should be met for 2σ. As seen in the plots of Fig. 48, the autoflare control law successfully lands the aircraft and meets all requirements.

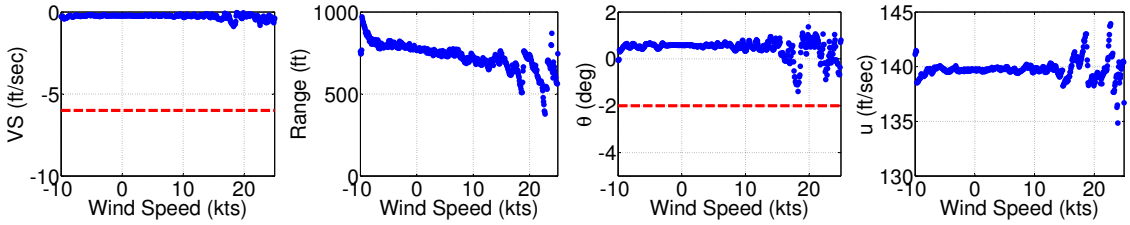

Fig. 48. PI Automatic Flare Turbulence Simulation

The Monte Carlo simulation for turbulence, as displayed in Fig. 48, show that the control laws provide a smooth touchdown in the presence of turbulence for all cases considered. The touchdown vertical velocity average was -0.33 ft/sec with a standard deviation of 0.13 ft/sec. The average speed of the aircraft was 139.0 ft/sec with a standard deviation of 1.01 ft/sec. The average range traveled during the flare was 526 ft with a standard deviation of 80.4 ft. The average pitch attitude angle at touchdown was 0.53 deg with a standard deviation of 0.35 deg. These simulations show good performance robustness to turbulence for the nominal plant.

Testing the model uncertainty of the autoflare control laws resulted in 100% successful landings with an average touchdown vertical speed of -0.73 ft/sec and a standard deviation of 0.26 ft/sec for the case with still air. When tested in turbulent air, 16% of the cases were soft landings, 16% were hard landings, and 67% were damage landings. The average vertical speed was -15 ft/sec with a standard deviation

of 9.3 ft/sec. The average distance traveled during the flare was 109 ft with a standard deviation of 278 ft. The average pitch attitude angle was -5.4 deg with a standard deviation of 9.4 deg. The average speed of the aircraft at touchdown was 151.2 ft/sec with a standard deviation of 6.67 ft/sec. From the model uncertainty robustness simulations, the autoflare control law is robust to model uncertainties when in still air, but is not robust to model uncertainties when in moderate turbulence.

The simulations presented above show that the control laws designed using the PI technique provide good performance and are robust to turbulence for the nominal plant, but only robust to model uncertainties when turbulence is not present. As turbulence increases, the performance robustness of the control laws to model uncertainties decreases significantly.

Results from the turbulence Monte Carlo simulations for the automatic flare are summarized in Table XIV and show that both controller types offer similar performance robustness to turbulence. As seen in Table XV, both the PI and QFT controllers exhibit good performance robustness to model uncertainties in still air, but in turbulence, the QFT controller offers significantly better performance robustness.

The simulations for the QFT controller prove that this design technique is as capable as the PI controller for an approach and landing controller with comparable performance, and the QFT controller offers better performance robustness to turbulence and model uncertainties.

Table XIV. Autoflare Controller Turbulence Comparison

Performance Metric	QFT	PI
Percent Soft Landings (%)	99.6	100
Percent Hard Landings (%)	0.4	0
Percent Damage Landings (%)	0	0
VS_{TD} Average (ft/sec)	-0.52	-0.27
VS_{TD} Standard Deviation (ft/sec)	0.91	0.12
d_{flare} Average (ft)	669	728
d_{flare} Standard Deviation (ft)	223	82
θ_{TD} Average (deg)	0.08	0.45
θ_{TD} Standard Deviation (deg)	0.93	0.36
u_{TD} Average (ft/sec)	141	141
u_{TD} Standard Deviation (ft/sec)	2.59	0.84

Table XV. Autoflare Controller Model Uncertainty Comparison

Performance Metric	Still Air		Turbulence	
	QFT	PI	QFT	PI
Percent Soft Landings (%)	100	100	96	16
Percent Hard Landings (%)	0	0	1	16
Percent Damage Landings (%)	0	0	2	67
VS_{TD} Average (ft/sec)	-0.14	-0.73	-0.52	-15.3
VS_{TD} Standard Deviation (ft/sec)	0.02	0.26	0.99	9.3
d_{flare} Average (ft)	922	420	669	109
d_{flare} Standard Deviation (ft)	150	57	223	278
θ_{TD} Average (deg)	0.6	1.65	0.1	-5.4
θ_{TD} Standard Deviation (deg)	0.21	0.06	0.93	9.4
u_{TD} Average (ft/sec)	140	141	145	151
u_{TD} Standard Deviation (ft/sec)	0.91	0.95	5.06	6.67

CHAPTER VII

CONCLUSIONS

This paper has developed control laws using the Quantitative Feedback Theory (QFT) technique and compared them to a Proportional-Integral (PI) baseline controller for the approach and landing control of a light twin engine aircraft, which has dynamics that are representative of a medium size unmanned aerial vehicle. The aircraft model was determined using system identification, and verified by comparing responses of the original nonlinear dynamics to the identified linear model. Using QFT direct digital design, controllers were developed for the localizer tracker, glideslope tracker, and automatic flare, as well as the inner-loops associated with each of these. The effects and interactions of the outer-loops using QFT were also investigated. The following conclusions are made based on this work:

1. For the localizer, glideslope, and automatic flare loops, the QFT controller provides good performance, and meets all specifications 100% of the time for the nominal plant in still air and in turbulent air. Results for the PI controller were similar. Regarding disturbance accommodation, the QFT controller exhibits good performance robustness to turbulence for the nominal plant, meeting the specifications for wind speeds from a 10 knot tailwind to a 25 knot headwind 99.6% of the time. The PI controller offered a similar level of performance robustness to turbulence.

2. The QFT and proportional-integral controllers both show good performance robustness to model uncertainties in still air, meeting the specifications 100% of the time. However, in turbulent air the QFT controller provides significantly better all around performance robustness. For the localizer, the QFT controller

is able to meet the specifications 70% of the time, versus 14% of the time for the PI controller. The glideslope QFT controller meets the specifications 88% of the time, versus 42% of the time for the PI controller. Finally, the automatic flare QFT controller produced soft landings 97% of the time, versus 16% of the time for the PI controller. This feature is particularly important for safe and survivable landing operations.

3. When simulating sensor characteristics for an Instrument Landing System (ILS), Microwave Landing System (MLS), and Global Positioning System (GPS), both the QFT and PI controllers showed similar levels of performance robustness in still air, with the exception of the GPS approach. Because of the large errors in estimating altitude, the QFT controller resulted in success 94.0% of the time, and the PI controller resulted in success 66.8% of the time. In turbulent air, the QFT controller showed significantly better results for all three approach types simulated. The QFT localizer tracker resulted in a successful approach 97.4%, 100%, and 100% of the time for ILS, MLS, and GPS, respectively. The PI localizer tracker provided successful approaches 60.4%, 66.8%, and 37.2% of the time for ILS, MLS, and GPS approaches, respectively. The QFT glideslope tracker showed successful approaches for ILS, MLS, and GPS approaches 94.2%, 99.4%, and 80.6% of the time, respectively. The PI glideslope tracker resulted in successful approaches for ILS, MLS, and GPS approaches 53.0%, 57.2%, and 27.8% of the time, respectively.

4. Based on the results presented in this paper, the QFT controller is judged to offer better overall performance robustness to model uncertainties and sensor noise, particularly when turbulence is present.

CHAPTER VIII

RECOMMENDATIONS

This chapter presents recommendations to further the work presented for QFT and PI automatic landing control laws. If this design were to be flight tested, more work would be needed to evaluate and implement the control laws. The following is recommended:

1. The effect of crosswinds on controller performance need to be evaluated before the controller is flight tested. In practice, it is common for an autopilot to have an algorithm that estimates crosswinds based on various flight parameters. The crosswinds are canceled by using integral control on the localizer tracker control loop; however, for each different magnitude of crosswind, a different integral gain is needed. Typically, the integral gain is scheduled with crosswind magnitude. Further investigation is needed to determine if the QFT controller would compensate for crosswinds, or if modification of the control laws is necessary.

2. To evaluate as many real-world conditions as is feasible, and for specific applications, additional Monte Carlo simulations could be conducted using various combinations of sensor characteristics, turbulence, and model uncertainties.

3. Real-time simulation should be conducted to further evaluate the designed control laws. Testing with real-time simulation that includes turbulence as well as sensor noise will help verify the control laws.

REFERENCES

[1] B. L. Stevens and F. L. Lewis, *Aircraft Control and Simulation*, Wiley-Interscience, New York, 1992.

[2] J. H. Blakelock, *Automatic Control of Aircraft and Missiles*, Wiley-Interscience, New York, 1991.

[3] K. Nho and R. K. Agarwal, "Automatic landing system design using fuzzy logic," *Journal of Guidance, Control, and Dynamics*, vol. 23, no. 2, pp. 298–304, February 2000.

[4] J. Juang and W. Chang, "Intelligent automatic landing system using time delay neural network controller," *Applied Artificial Intelligence*, vol. 17, no. 7, pp. 563–581, 2003.

[5] S. Shue and R. K. Agarwal, "Design of automatic landing systems using mixed H_2/H_∞ control," *Journal of Guidance, Control, and Dynamics*, vol. 22, no. 1, pp. 103–114, January-February 1999.

[6] D. Kim, Y. Choi, and J. Suk, "A glidepath tracking algorithm for autolanding of a UAV," in *Infotech@Aerospace*, Arlington, VA, 26–29 September 2005, AIAA paper 2005-6979.

[7] M. Attar, E. Wahnon, and D. Chaimovitz, "Advanced flight control technologies for UAVs," in *2nd AIAA Unmanned Unlimited Systems, Technologies, and Operations*, San Diego, CA, 15–18 September 2003, AIAA paper 2003-6537.

[8] Cloud Cap Technology, "Piccolo autopilot," www.cloudcaptech.com, 2006.

[9] Procerus Technologies, "Kestrel autopilot," www.procerusuav.com, 2006.

[10] G. Loegering and S. Harris, "Landing dispersion results – global hawk autoland system," in *AIAA's 1st Technical Conference and Workshop on Unmanned Aerospace Vehicles*, Portsmouth, VA, 23–20 May 2002, AIAA paper 2002-3457.

[11] R. W. Davidson, "Flight control design and test of the joint unmanned combat air system J-UCAS X-45A," in *AIAA 3rd "Unmanned-Unlimited" Technical Conference, Workshop, and Exhibit*, Chicago, IL, 20–23 September 2004, AIAA paper 2004-6557.

[12] D. Wood, "X-47A pegasus flight and mission systems design and test," in *AIAA 2nd "Unmanned Unlimited" Systems, Technologies, and Operations*, San Diego, CA, 15–18 September 2003, AIAA paper 2003-6628.

[13] Sierra Nevada Corporation, "Millimeter-wave beacon tracking system," www.sncorp.com/uav.html, 2006.

[14] C. H. Houpis and S. J. Rasmussen, *Quantitative Feedback Theory Fundamentals and Applications*, Marcel Dekker, New York, 1999.

[15] O. Yaniv, *Quantitative Feedback Design of Linear and Nonlinear Control Systems*, Kluwer Academic Publishers, Boston, 1999.

[16] I. Horowitz, "Application of quantitative feedback theory (QFT) to flight control problems," in *IEEE Conference on Decision and Control*, Honolulu, HI, December 1990.

[17] D. E. Bossert, "Design of robust quantitative feedback theory controllers for pitch attitude hold systems," *Journal of Guidance, Control, and Dynamics*, vol. 17, no. 1, pp. 217–219, 1994.

[18] S. F. Wu, M. J. Grimble, and S. G. Breslin, "Introduction to quantitative feedback theory for lateral robust flight control systems design," *Control Engineering Practice*, vol. 6, no. 7, pp. 805–828, July 1998.

[19] S. N. Sheldon and S. J. Rasmussen, "Development and first successful flight test of a QFT flight control system," in *National Aerospace and Electronics Conference*, Dayton, OH, January 1994.

[20] P. L. Fontenrose and C. E. Hall Jr., "Development and flight testing of quantitative feedback theory pitch rate stability augmentation system," *Journal of Guidance, Control, and Dynamics*, vol. 19, no. 5, pp. 1109–1115, September-October 1996.

[21] J. Roskam, *Airplane Flight Dynamics and Automatic Flight Controls II*, DAR-Corporation, Lawrence, KS, 2003.

[22] Anon., "Instrument flying handbook," Tech report, FAA-H-9093-15, Federal Aviation Administration, 2001.

[23] J. Valasek and W. Chen, "Observer/kalman filter identification for online system identification of aircraft," *Journal of Guidance, Control, and Dynamics*, vol. 26, no. 2, pp. 347–353, March-April 2003.

[24] Rockwell International, *Rockwell Commander 700 Pilots Operating Handbook*, 1979.

[25] C. E. Lan and J. Roskam, *Airplane Aerodynamics and Performance*, Roskam Aviation and Engineering, Lawrence, KS, 1980.

[26] Anon., "Aerospace blockset dryden wind turbulence model help," MATLAB 7.0 help, The Mathworks, Natick, MA, 2006.

[27] Anon., "Military standard flying qualities of piloted aircraft," MIL-STD-1797a, Department of Defense, Washington, DC, March 1990.

[28] J. Roskam, *Airplane Flight Dynamics and Automatic Flight Controls I*, DAR-Corporation, Lawrence, KS, 2003.

[29] J. Valasek, "AERO 625 course notes," Class Notes, Texas A&M University, 1998.

[30] Anon., *MATLAB 7.0 Software*, The Mathworks, Natick, MA, 2005.

[31] G. Franklin, J. D. Powell, and M. L. Workman, *Digital Control of Dynamic Systems*, Addison-Wesley, Menlo Park, CA, 1998.

[32] Anon., "Flight control systems - design, installation and test of piloted aircraft, general specification for," MIL-STD-9490D, Department of Defense, Washington, DC, 1964.

[33] D. B. Ridgely, S. S. Banda, T. E. McQuade, and P. J. Lynch, "Linear-quadratic-gaussian with loop-transfer-recovery methodology for an unmanned aircraft," *Journal of Guidance, Control, and Dynamics*, vol. 10, no. 1, pp. 82–89, January 1987.

[34] C. Borghesani, Y. Chait, and O. Yaniv, *QFT Frequency Domain Control Design Toolbox Software*, Terasoft, San Diego, CA, 2003.

[35] Jeppesen Company, *Jeppesen Airway Manual Services*, Instrument Approach Plates, Englewood, CO, 2006.

[36] Anon., "2001 federal radionavigation systems," DOT-VNTSC-RSPA-01-3.1/DOT-4650.5, US Department of Defense and US Department of Transportation, Springfield, VA, 2001.

[37] R. W. Rissmiller Jr., "Microwave landing system: A pilots point of view," *IEEE Aerospace and Electronic Systems Magazine*, vol. 5, no. 5, pp. 47–49, 1990.

[38] J. B. Feather and B. K. Craven, "Microwave landing system autoland system analysis," NASA Contractor Report NASA-CR-189551, Douglas Aircraft Co., Long Beach, CA, December 1991.

[39] R. Brown, G. Romrell, G. Johnson, D. Kaufmann, and X. Qin, "DGPS category IIIb automatic landing system flight test results," in *Proceedings of the IEEE PLANS, Position Location and Navigation Symposium*, Atlanta, GA, 22–26 April 1996.

[40] L. S. Monteiro, "What is the accuracy of DGPS?," in *Proc. of the Annual Meeting - Institute of Navigation*, Cambridge, MA, 2005.

[41] P. Enge, T. Walter, S. Pullen, C. Kee, Y. Chao, and Y. Tsai, "Wide area augmentation of the global positioning system," *Proceedings of the IEEE*, vol. 84, no. 8, pp. 1063–1088, 1996.

[42] P. Enge, "Local area augmentation of GPS for the precision approach of aircraft," *Proceedings of the IEEE*, vol. 87, no. 1, pp. 111–132, 1999.

APPENDIX A

CONTROL LAW BLOCK DIAGRAMS

This Appendix contains the control law block diagrams for each control loop designed for both the PI controller and the QFT controller.

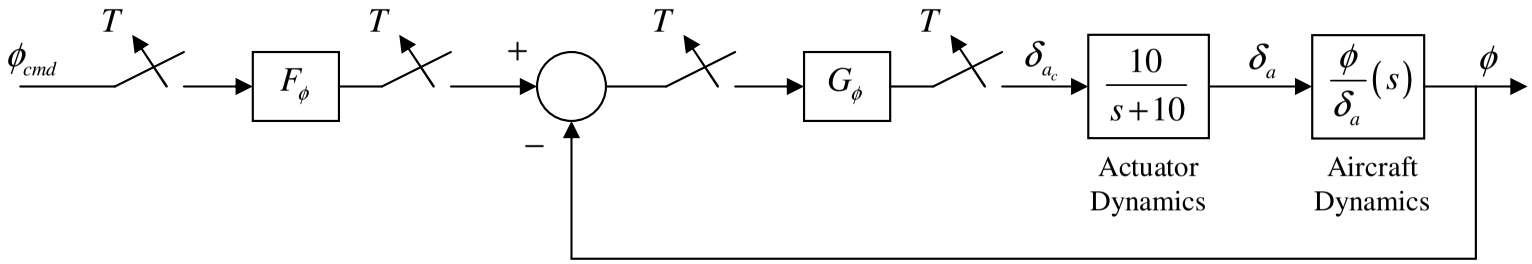

$$G_\phi = \frac{1.039(z-0.8484)}{(z-0.8021)}$$

$$F_\phi = \frac{0.23834(z^2-1.692z+0.7331)}{(z^2-1.853z+0.8633)}$$

$$T = 0.1 \text{ sec}$$

Fig. 49. QFT Bank Angle Command and Hold Block Diagram

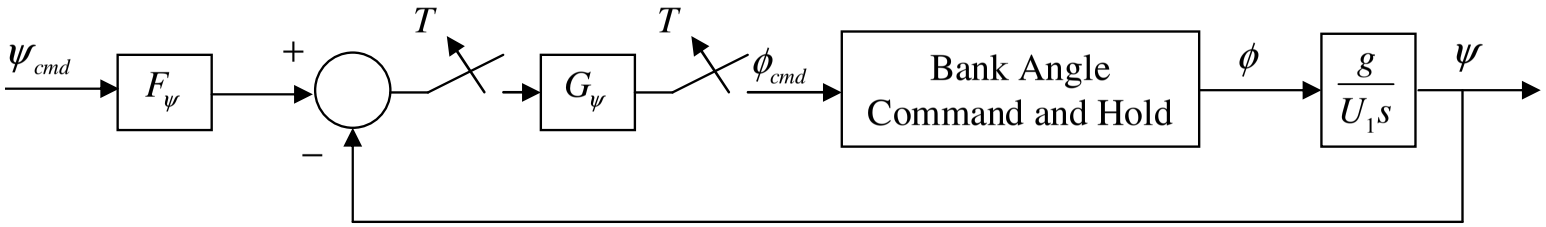

$$G_\psi = 0.902$$
$$F_\psi = 1$$
$$g = 32.2 \text{ ft/sec}^2$$
$$U_1 = 151.9 \text{ ft/sec}$$
$$T = 0.1 \text{ sec}$$

Fig. 50. QFT Heading Angle Command and Hold Block Diagram

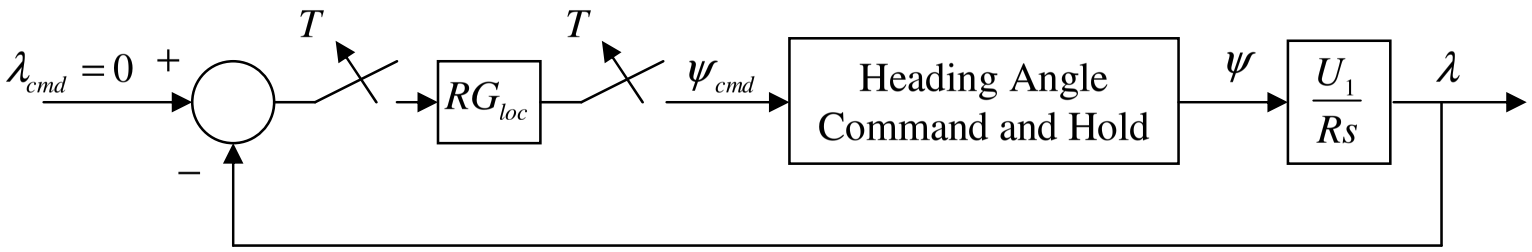

$$G_{loc} = \frac{0.001268(z - 0.9891)}{(z - 0.9766)}$$

$$U_1 = 151.9 \text{ ft/sec}$$

$$R = \text{ range in ft}$$

$$T = 0.1 \text{ sec}$$

Fig. 51. QFT Localizer Tracker Block Diagram

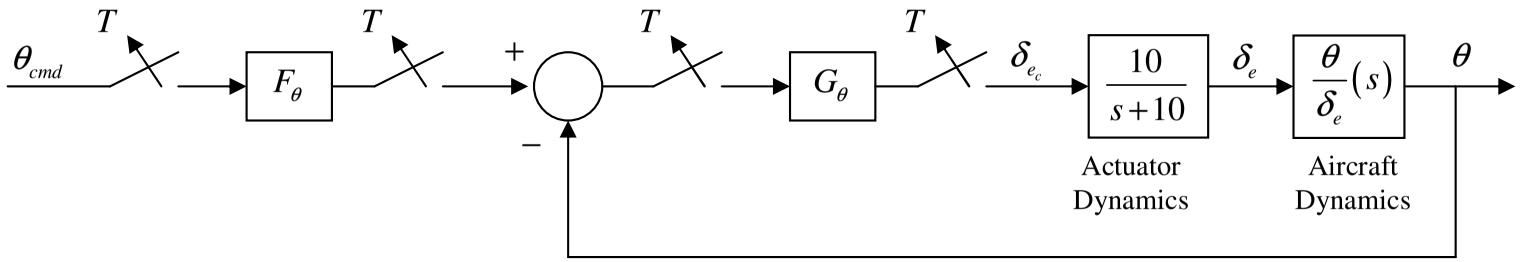

$$G_\theta = \frac{0.85254(z-0.9581)(z-0.9546)}{(z-1)(z-0.7762)}$$

$$F_\theta = \frac{0.18902(z-0.5434)}{(z-0.9128)}$$

$$T = 0.1 \text{ sec}$$

Fig. 52. QFT Pitch Angle Command and Hold Block Diagram

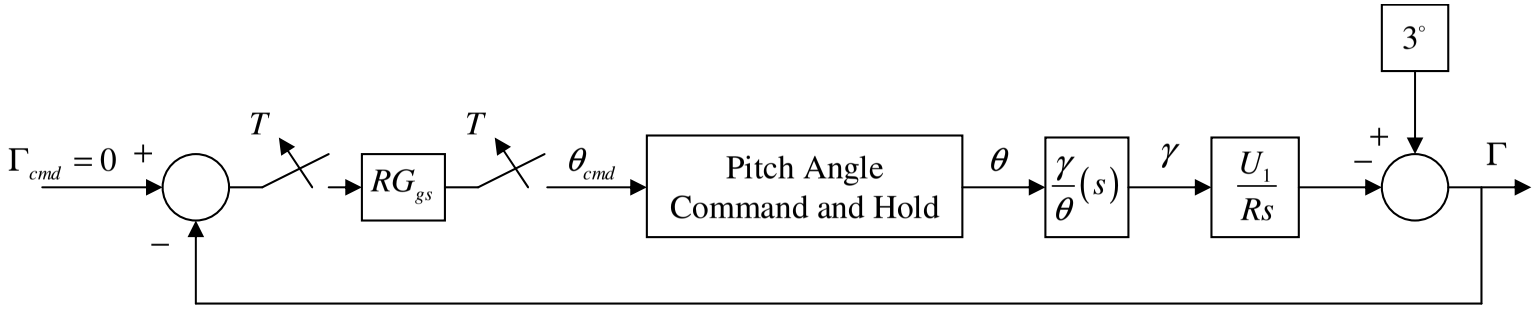

$$G_{gs} = \frac{0.00264(z-0.9899)(z-0.9957)(z-0.9826)}{(z-1)(z-0.9857)(z-0.9772)}$$

$U_1 = 151.9$ ft/sec

$R =$ range in ft

$T = 0.1$ sec

Fig. 53. QFT Glideslope Tracker Block Diagram

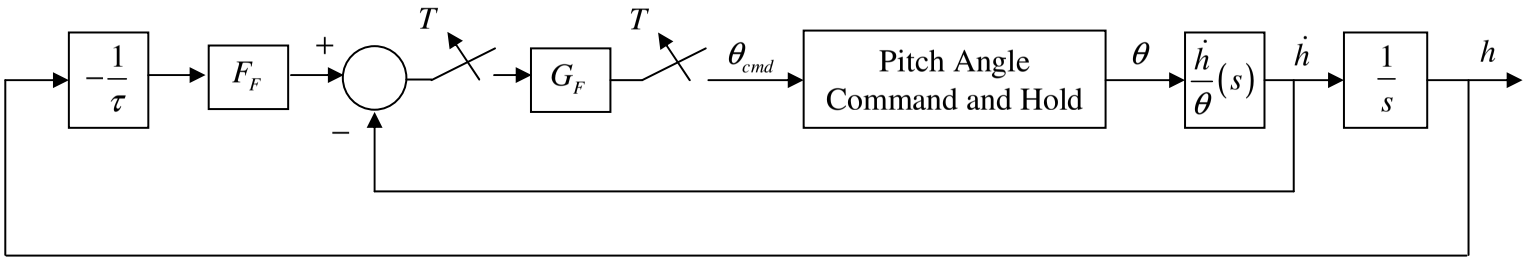

$$G_F = \frac{0.0769(z-0.9376)(z-0.8733)}{z(z-1)}$$

$$F_F = 1$$

$$\tau = 1.99 \text{ sec}$$

$$T = 0.1 \text{ sec}$$

Fig. 54. QFT Automatic Flare Block Diagram

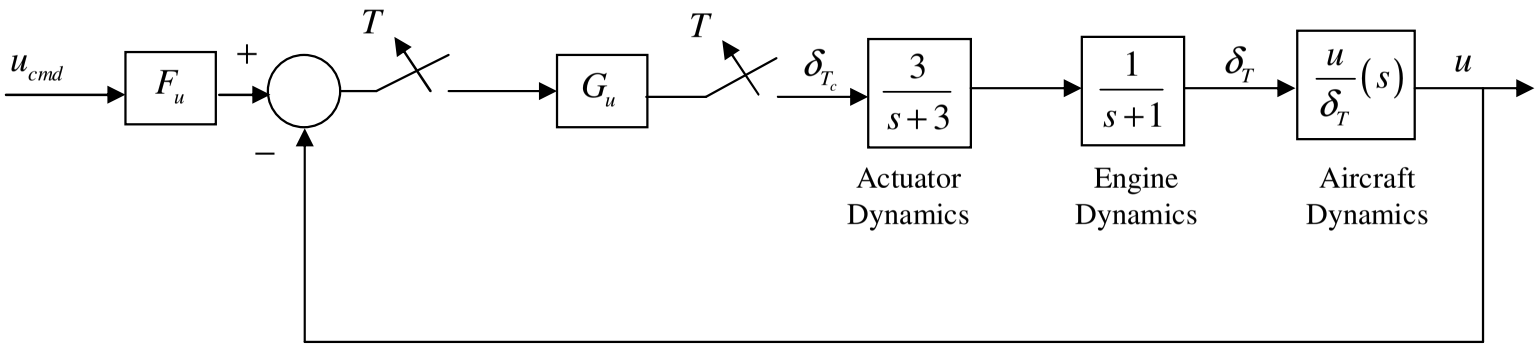

$$G_u = \frac{3.988(z-0.972)(z-0.938)}{(z-1)(z-0.9803)}$$

$$F_u = 1$$

$$T = 0.1 \text{ sec}$$

Fig. 55. QFT Airspeed Command and Hold Block Diagram

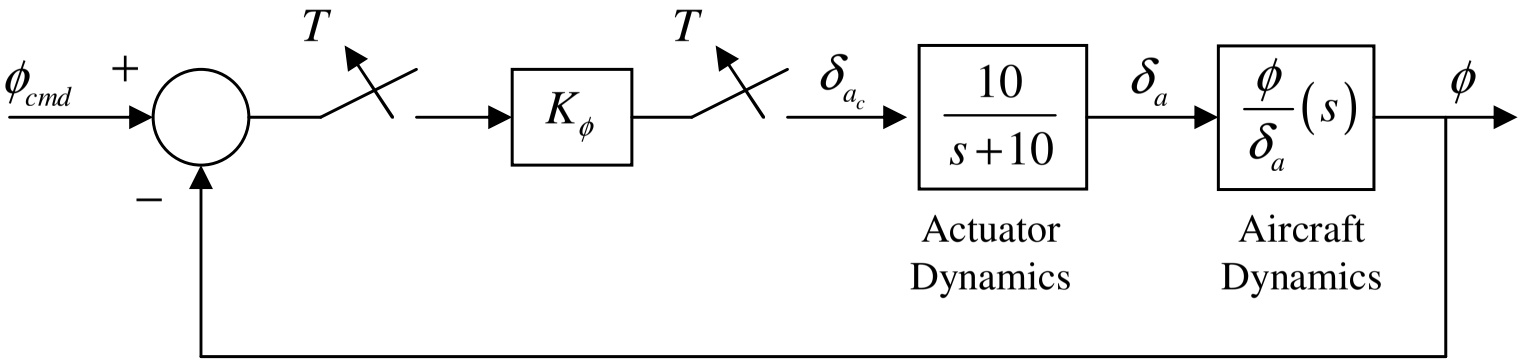

$$K_\phi = -0.6$$

$$T = 0.1 \text{ sec}$$

Fig. 56. PI Bank Angle Command and Hold Block Diagram

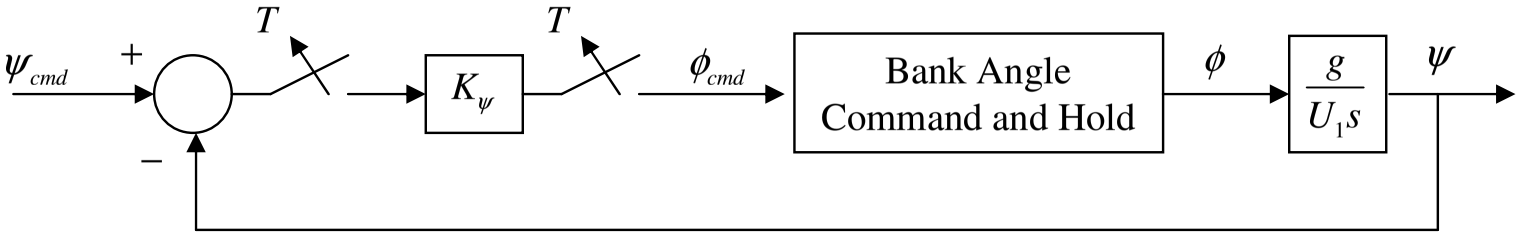

$$K_\psi = 1.1$$
$$g = 32.2 \text{ ft/sec}^2$$
$$U_1 = 151.9 \text{ ft/sec}$$
$$T = 0.1 \text{ sec}$$

Fig. 57. PI Heading Angle Command and Hold Block Diagram

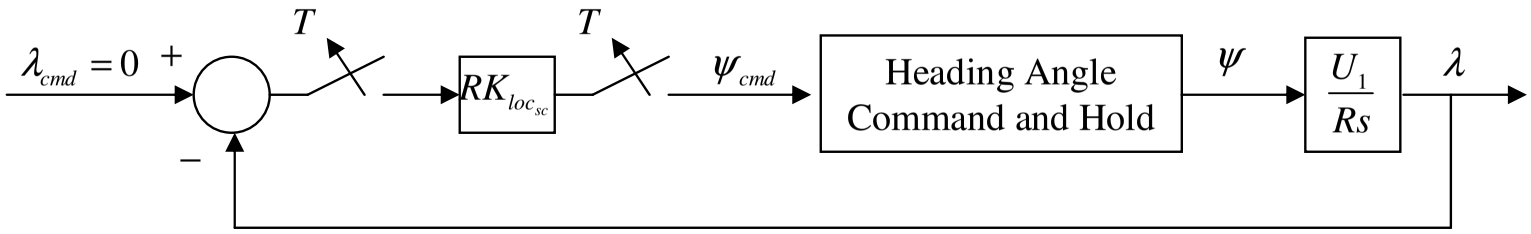

$$K_{loc_{sc}} = 0.0003$$

$$U_1 = 151.9 \text{ ft/sec}$$

$$R = \text{ range in ft}$$

$$T = 0.1 \text{ sec}$$

Fig. 58. PI Localizer Tracker Block Diagram

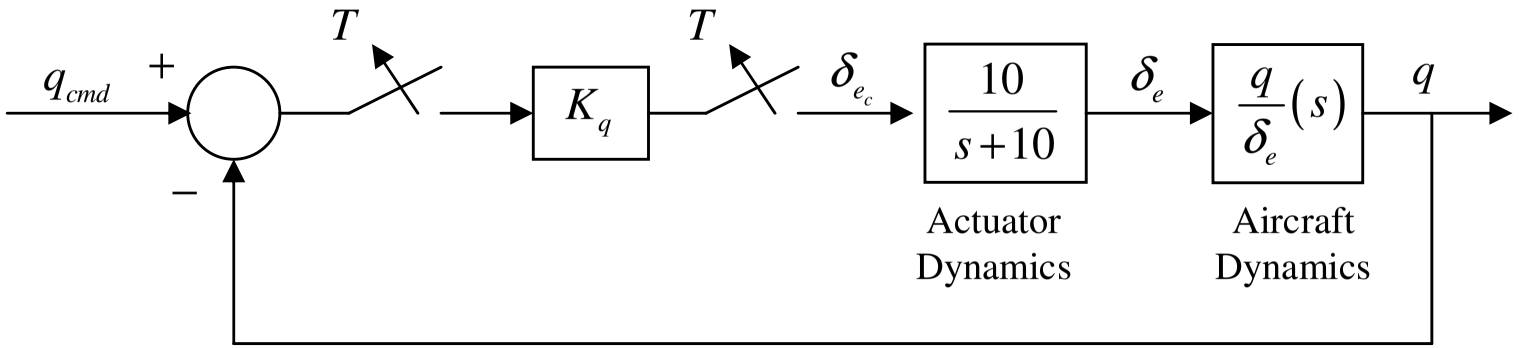

$$K_q = 0.164$$

$$T = 0.1 \text{ sec}$$

Fig. 59. PI Pitch Damper Block Diagram

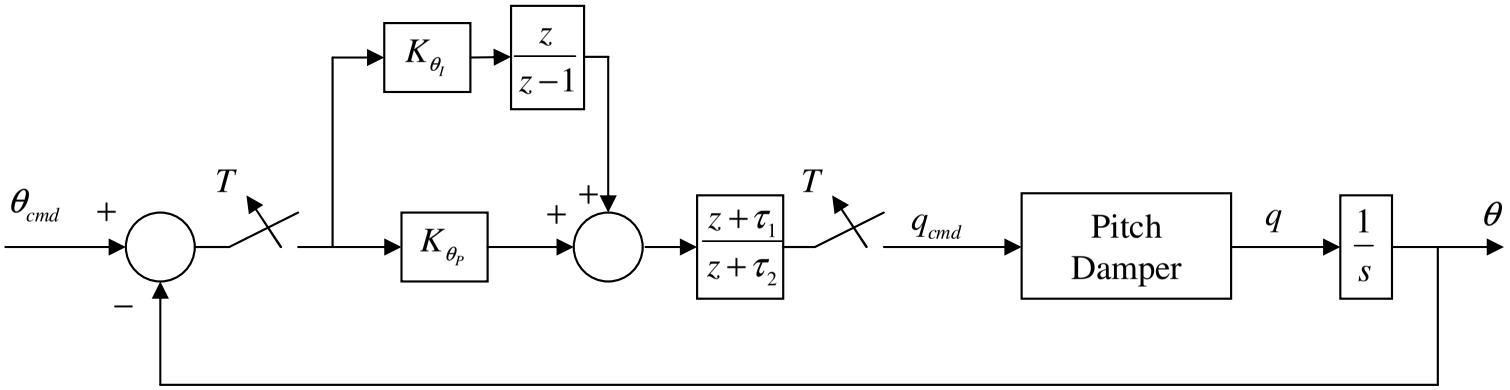

$$K_{\theta_P} = 0.252$$
$$K_{\theta_I} = 1.0$$
$$\tau_1 = 0.983$$
$$\tau_2 = 0.0136$$
$$T = 0.1 \text{ sec}$$

Fig. 60. PI Pitch Angle Command and Hold Block Diagram

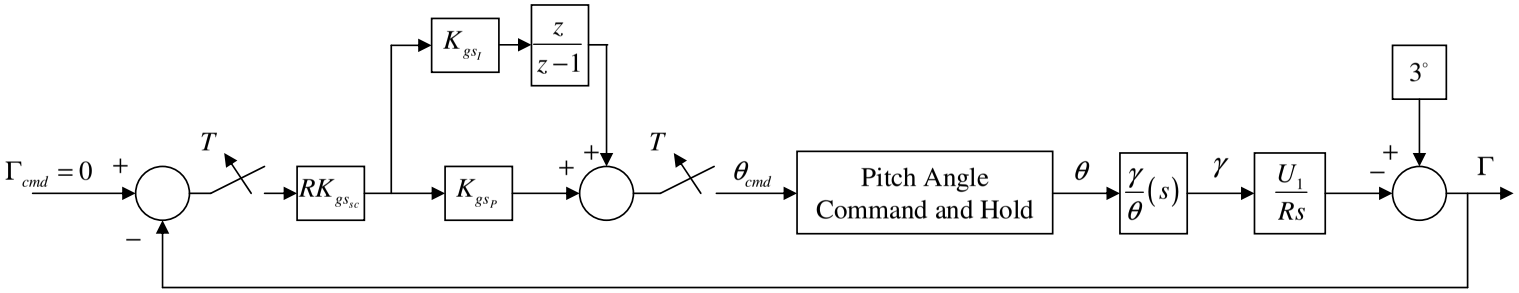

$K_{gs_{sc}} = 0.003$

$K_{gs_P} = 1.0$

$K_{gs_I} = 0.01$

$U_1 = 151.9$ ft/sec

$R =$ range in ft

$T = 0.1$ sec

Fig. 61. PI Glideslope Tracker Block Diagram

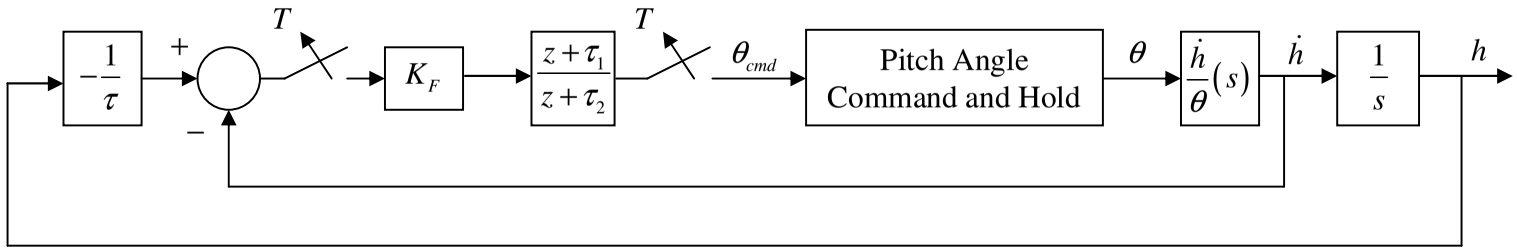

$$K_F = 7.0$$
$$\tau_1 = 0.91$$
$$\tau_2 = 0.0697$$
$$\tau = 1.99 \text{ sec}$$
$$T = 0.1 \text{ sec}$$

Fig. 62. PI Automatic Flare Block Diagram

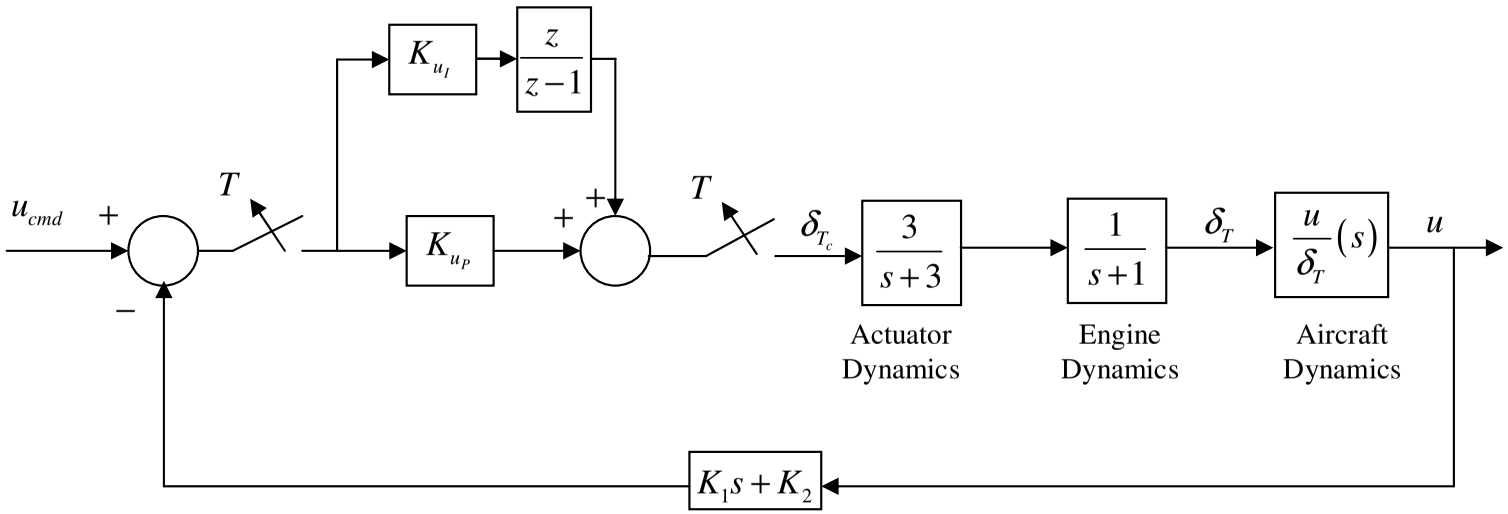

$$K_{u_P} = 0.025$$
$$K_{u_I} = 1.0$$
$$K_1 = 5.0$$
$$K_2 = 1.0$$
$$T = 0.1 \text{ sec}$$

Fig. 63. PI Airspeed Command and Hold Block Diagram

VITA

Thomas William Wagner, Jr. graduated from Klein Oak High School in Spring, Texas. He subsequently attended Texas A&M University, where he received his Bachelor of Science in aerospace engineering (2004) and Master of Science in aerospace engineering (2007). Upon completion of his graduate degree, he was chosen a pilot candidate in the United States Air Force. He may be contacted via the following address:

11425 Upland Way

Gravette, AR. 72736